Article

Not peer-reviewed version

# Possible Influence of Brittle Tectonics on the Main Road Network Built in the Central African Environment

Sandra Céleste TCHATO *, Blaise Pascal Gounou Pokam, Marthe Mbond Ariane Gweth, Euloge Felix Kayo Pokam, Michel André Pouth Nkoma, Ibrahim Mboumbouo Ngapouth, Yvonne Poufone Koffi, Eliezer Manguelle-Dicoum, Philippe Njandjock Nouck

Posted Date: 29 August 2023

doi: 10.20944/preprints202308.1946.v1

Keywords: Sustainable planning; sustainable monitoring; remote sensing; GIS; lineaments; fault; fracture

*Article*

# Possible Influence of Brittle Tectonics on the Main Road Network Built in the Central African Environment

**Sandra Céleste Tchato [1,2,*], Blaise Pascal Gounou Pokam [3], Marthe Mbond Ariane Gweth [1], Euloge Felix Kayo Pokam [4], André Michel Pouth Nkoma [1], Ibrahim Mbouombouo Ngapouth [1], Yvonne Poufone Koffi [1,5], Eliezer Manguelle-Dicoum [1] and Philippe Njandjock Nouck [1]**

[1] Department of Physics, University of Yaoundé I, P.O. Box 812, Yaoundé, Cameroon
[2] Geodesy Research Laboratory, National Institute of Cartography, Yaoundé, Cameroon
[3] Department of Civil-engineer, University of Ngaoundéré, Ngaoundéré 237, Cameroon
[4] Department of Mathematical economics and econometrics, Omar Bongo University, Bo 13113 Libreville, Gabon
[5] Laboratory of Image Processing, National Institute of Cartography, Yaoundé
* Correspondence: sandra_tchato77@yahoo.com

**Abstract:** The construction of sustainable road and highway networks in the world, despite numerous feasibility, pre-feasibility and execution studies, are always confronted with the demands and vagaries of foreseeable and unforeseeable natural disasters. Studying cyclones, earthquakes, fracturing and landslide zones along roads is therefore a challenge for the sustainability of these infrastructures. In many countries around the world, the methods generally used for these studies are not only expensive and time-consuming, but the results obtained are not always efficient. This work examines whether Landsat 8 (with a high cloud level) and SRTM data can be used in both equatorial and coastal Central Africa zones to produce relevant mapping, locating fracture and landslide zones, in order to contribute not only to better road layout at lower cost and in a relatively short time, but also to better prevention of geological disasters that may occur on its network. To this end, a map of the main road network was produced and validated with field data, as well as the maps of the main unstable slopes, faults and fractures zones intersecting the road or highway network. These approaches are useful for sustainable planning, management, monitoring and extension of roads worldwide especially, in Central Africa.

**Keywords:** sustainable planning; sustainable monitoring; remote sensing; GIS; lineaments; fault; fracture

## 1. Introduction

Roads and corridors where construction interacts with both the environment and ecosystems, have been means of communication and exchange between nations, peoples and civilisations since antiquity. And to ensure their sustainable use, they are the subject of numerous studies (sociological, scientific, technical, anthropological and many others). However, the elements (bridges, pavements, tunnels, scuppers, embankments) of a road or corridor built sometimes at very high cost (whose average price per kilometre is between 336,944 $ to 4,930,885 $ in Central Africa [1–4]) are threatened by faulting and landslides.

These movements are one of the most destructive natural phenomena of infrastructure in the world and Africa is not spared. All over the world in general and in Central Africa in particular, the phenomenon is not to be neglected, as Figures 1 and 2 show that the road network is intercepted by faults and fractures, causing significant damages not only to houses, but also to road infrastructure and human lives, and therefore to socio-economic development. Although not widely reported in Central Africa, these movements are very recurrent and produce scouring of culverts, collapse of

 doi:10.20944/preprints202308.1946.v1



structures (bridges, scuppers, etc.) [5], and landslides (Figure 1) [6–8], slope failure, as studied in the work of Biswas et al [9] and Mbouombouo et al [10] in which it is established that slopes become unstable for slope values greater than $6.17^0$ in sandy-clay formations and for slope values greater than $10^0$ in gneissic formations respectively. Figure 1, based on the literature review, shows that roads are generally subject to rockfalls, collapses (longitudinal and transverse) and shears (longitudinal and transverse), which very often precede collapses. However, geological information does not always indicate the presence of several faults in the study area (Figure 2), yet according to the work of Aretouyap et al, Gweth et al, and Nguemhe et al, [8,11,12] there would be an enormous number of them. In the field, scientists need to know about fracturing to better orient the road network but due to many hazards such as vegetation cover, sedimentation, these faults and fractures are often hidden. The structural geology of an area has a significant influence on landslide occurrence and one way of integrating structural information into landslide risk assessment is through lineament mapping [13–18]. Lineaments can be defined as the surface expression of deep geological structures, usually corresponding to structural features such as geological contacts, foliations, schistosities, fold hinges, faults and fractures [19], which are structural lineaments. They may also correspond to man-made features (roads, pipelines, railways etc.) which are anthropogenic lineaments. Many studies have shown the importance of structural lineaments in land movement [8,20,21]. In addition, it is important to incorporate lineament density as it has proven to be effective in several fields of study, including geology, hydrogeology, geotechnics etc., in that it can highlight the most fractured areas, and therefore highlight areas with a particular anomaly [22–24].

Lineament extraction from geospatial data generally involves two approaches namely, the manual approach and the automatic approach, based on visual interpretation and the use of computer algorithms respectively [25]. In the manual approach, the extraction of lineaments is mainly influenced by the user's experience while the automatic approach mainly depends on the performance of the software used and the data provided in the image used [26]. Since the introduction of Landsat MSS in 1980, remote sensing has been widely used in lineament studies [25]. Indeed, remote sensing is a set of techniques used to acquire information about an area of the Earth's surface, without any physical contact with it. It allows the observation of very large and inaccessible areas in a short period of time, and therefore has a good ability to detect lithology, landforms and lineaments on imagery [27]. Several types of remote sensing images such as Landsat, IRS, LISS, ASTER, aerial photos and SPOT have been used for land movement assessment [25].

The geological maps available [28,29] show that there are nevertheless points where the road and fault networks meet in Central Africa. However, these maps do not provide a sufficient understanding of all the accidents such as landslides, shearing and collapses that occur on the aforementioned road network. Furthermore, Figure 2 shows that the fault network intercepts the road network in only 16 sectors, but in view of the many accidents recorded on these roads, it is clear that this map cannot be used to justify these numerous accidents. Landsat satellite images are often marred by a lot of cloud, which does not always allow good observation of the target [30,31]. In this work, the idea is to see whether by combining Landsat 8 images (for the 28 scenes used with cloud percentages of 0%, 0.31%, 3.24%, 6.02% and 46%) and DEM SRTM, we can achieve better mapping of accident-prone areas on these roads, and plan a sustainable layout for future infrastructure and, above all, better prevention and monitoring of disasters on the current road network. So, this work examines whether Landsat 8 OLI (Operational Land Imager) with a high cloud level and SRTM (Shuttle Radar Topographic Mapper) data can be used in both equatorial and coastal Central Africa zones to produce relevant mapping, locating fracture and landslide zones, in order to contribute not only to better road layout at lower cost and in a relatively short time, but also to better and sustainable prevention of geological disasters that may occur on these road network.

Preprints (www.preprints.org) | NOT PEER-REVIEWED | Posted: 29 August 2023 doi:10.20944/preprints202308.1946.v1



## 2. Study area

### *2.1. Geological setting*

The Precambrian basement complex of Central Africa which recorded the evolution of the crust from the Mesoarchean to the Neoproterozoic era [32,33] comprises two major units, namely the Pan-African Fold Belt and the Congo Craton (Ntem Complex).

In the study area, the Pan-African Fold Belt is subdivided into three domains, namely the Southern Domain, the Central Domain and the Northern Domain [34] (Figure 2).

(1) The southern domain is a huge allochthonous nappe unit bounded to the south by the Congo Craton, to the west by the Kribi-Campo fault and extending eastwards into the Central African Republic in the Bolé and Gbaya series [35]. It comprises high-grade metamorphic and igneous rock units, low to medium grade shales of sedimentary origin and metamorphosed Neoproterozoic metasediments under high pressure metamorphism [36]; (2) the central domain, which is bounded by the Sanaga Fault in the south and the Tcholliré-Banyo Fault in the north, includes the Adamaoua Fault and other anastomosing faults, constituting the N70E central Cameroonian shear zone system [37].

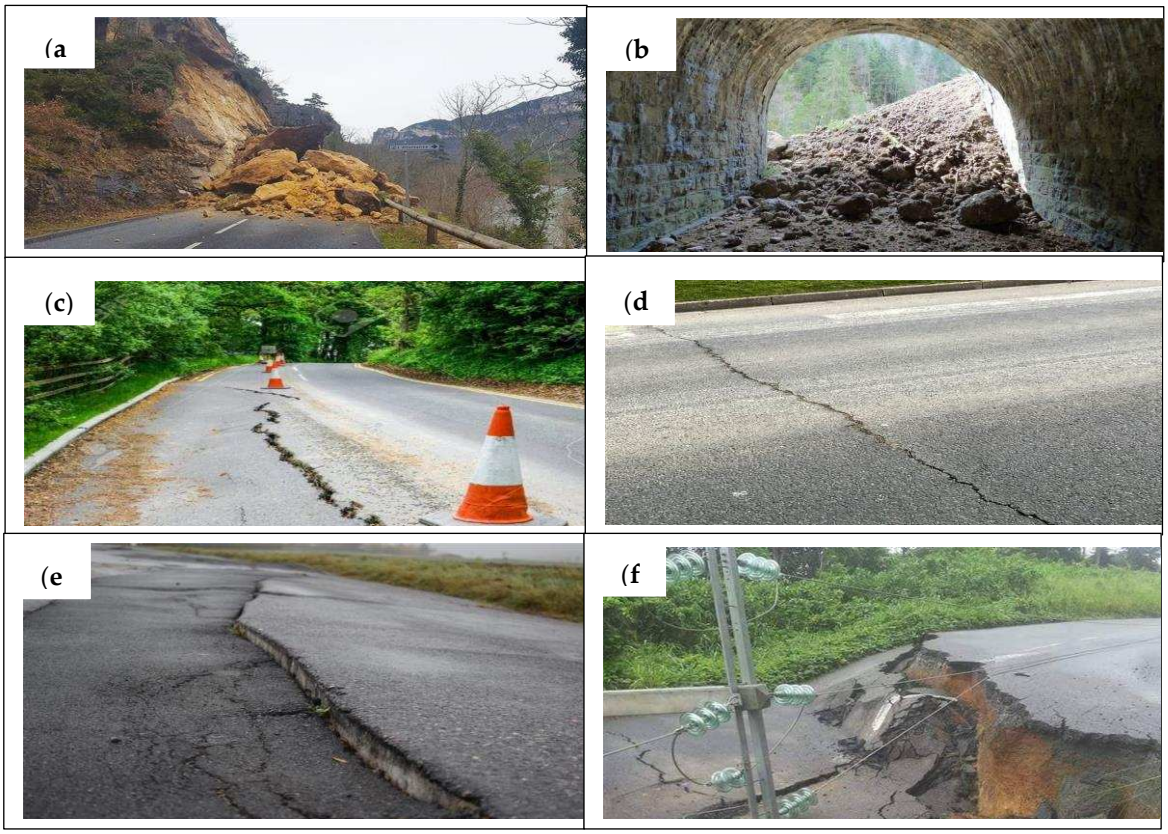


**Figure 1.** Images of some natural hazards on some roads. (**a**) Landslide on the road in the Gorges du Tarn [38], (**b**) Landslide in a tunnel [39], (**c**) Longitudinal shear of a road [40], (**d**) Transverse shear of a road [41], (**e**) Longitudinal collapse of a road [42], (**f**) Transverse collapse of a road [43].

This domain consists of Archean to Paleoproterozoic high-grade gneisses intruded by broad syntectonic Neoproterozoic plutonic rocks of calc-alkaline affinity with high potassium (K) content, with emplacement ages around 600 Ma [44–46]; (3) the northern domain located west of the Tchollire-Banyo fault and extending along the western border of Cameroon consists of: high-grade metamorphic complex, comprising rocks of volcano-sedimentary and sedimentary origin due to the presence of orthogneiss with predominant dioritic content; metasedimentary rocks from the Neoproterozoic schist belts; and predominantly calc-alkaline Pan-African granitoids deposited

Preprints (www.preprints.org) | NOT PEER-REVIEWED | Posted: 29 August 2023 doi:10.20944/preprints202308.1946.v1



between 660 and 580 Ma [47]. The volcanic rocks found there have tholeiitic and alkaline affinities. This area has experienced at least two episodes related to the Pan-African plutonism, the oldest of which, dated between 640 and 620 Ma, corresponds to pre- to syntectonic calc-alkaline granitoids and the youngest (580 Ma) corresponds to late-tectonic granitoids [48,49]. Three main successive tectonic events have been identified in this area by Ngako et al [50]: Crustal thickening (630-620 Ma); left lateral distortion movements (613-585 Ma), marked by the northern area shear zones and the Sanaga shear zone; right lateral distortion movements (585-540 Ma), marked by the northern area dextral shear zones and the central area shear zone.

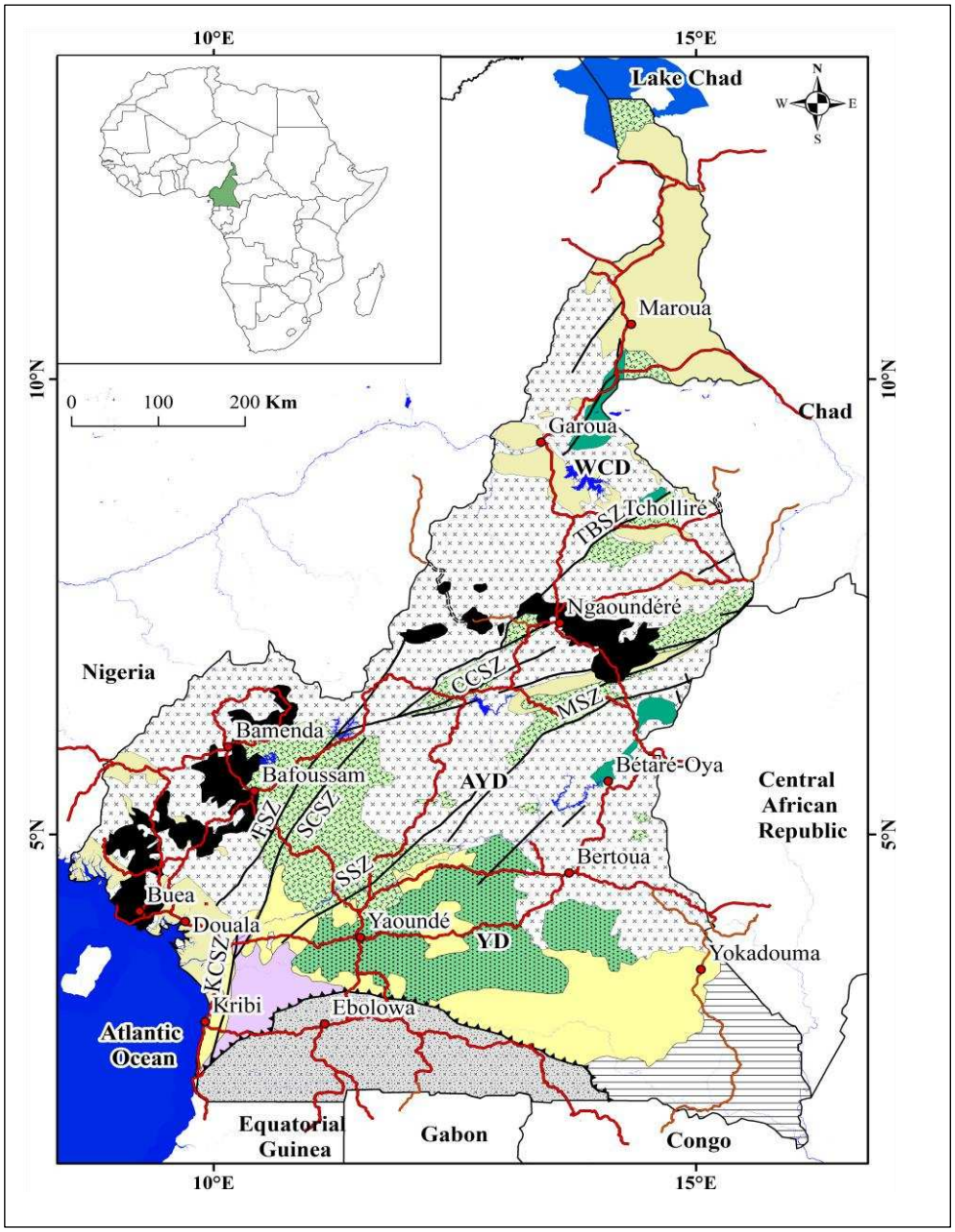

 doi:10.20944/preprints202308.1946.v1



**Figure 2.** Geological map of the study area modified from Kankeu et al. [51], showing the main lithotectonic domains. YD: Yaounde domain; AYD: Adamaoua-Yade domain; WCD: Western Cameroon domain; TBSZ: Tchollire-Banyo shear zone; CCSZ: Central Cameroon shear zone; KCSZ: Kribi-Campo shear zone; MSZ: Meiganga shear zone; SSZ: Sanaga shear zone; SCSZ: South Cameroon shear zone; FSZ: Foumban shear zone.

The Ntem Complex representing the northern part of the Congo Craton is subdivided into three units: the Ntem Unit, the Nyong Unit and the Ayna Unit.

The Ntem Unit consists mainly of younger intrusive complexes, banded series and greenstone belts. The intrusive complexes include the tonalitic, trondjemite and granodiorite suites constituting the TTG (Tonalite-Trondjemite-Granodiorite) suite [52], and the charnokitic-magmatic suite [53]. The banded series consists of granitic gneisses, charnokitic gneisses, enderbergites and leptynites [54]. The banded iron formation (BIF), metagraywackes, pyroxenites, sillimanite paragneiss and garnet amphibolites constitute the greenstone belts [55].

The Nyong unit is a high-grade gneiss unit, dominated by biotite-hornblende gneisses locally occurring as grey TTG, charnockites, garnet-amphibole-pyroxenites and banded iron formations (BIF). The magmatic rocks found here (granodiorites, augen metadiorites, syenites) are represented by a SW-NE trending group of small intrusions [56].

Formed by crystallophyllian rocks, greenstone belts and intrusive granitoids [28], the Ayna unit comprises N120-N140E trending foliations superimposed by antepan-African folds and blastomylomites, and overlain by the Pan-African nappe [29].

The Ntem complex has experienced two major periods of deformation. The first period of deformation is marked by successive diapiric emplacement of the TTG and Mesoarchean charnockites, characterised by isoclinal stretching and folding, vertical lineation and foliation [52]; and the second one includes the development of N-S to NE-SW trending sinister shear zones, partial melting of the greenstone belt and TTG suite rocks, followed by granite formation [57].

### *2.2. Roads*

The study area extends geographically between latitudes 1°38'5 "N and 13°4'50.7 "N and longitudes 8°30'50.6 "E and 16°12'11.8 "E and has a surface area of 475442 km². There are 18 national roads in total, but taking into account the slip roads we can count 25, including N1, N1A, N2, N2A, N3, N4, N5, N6, N6A, N7, N8, N9, N10, N11, N12, N13, N13A, N14, N15, N15A, N16, N17, N17A, N17B and N18 (Figure 3a–c).

N1, N1A, N6 and N14 ensure trade between Cameroon and Nigeria; N1, N12, N13 and N13A connects Cameroon to Chad; N2 and N17B link Cameroon to Gabon; N2A and N7 join Cameroon to Equatorial Guinea; N9 connects Cameroon to Congo; N1 and N10 connect Cameroon to the Central African Republic. N3 is the main road linking the port area (from the Atlantic Ocean) to all the other countries in Central Africa. The other national roads are intermediate roads leading to N1A, N1, N2, N2A, N6, N7, N9, N10, N12, N13, N13A, N14 and N17B.

Preprints (www.preprints.org) | NOT PEER-REVIEWED | Posted: 29 August 2023 doi:10.20944/preprints202308.1946.v1



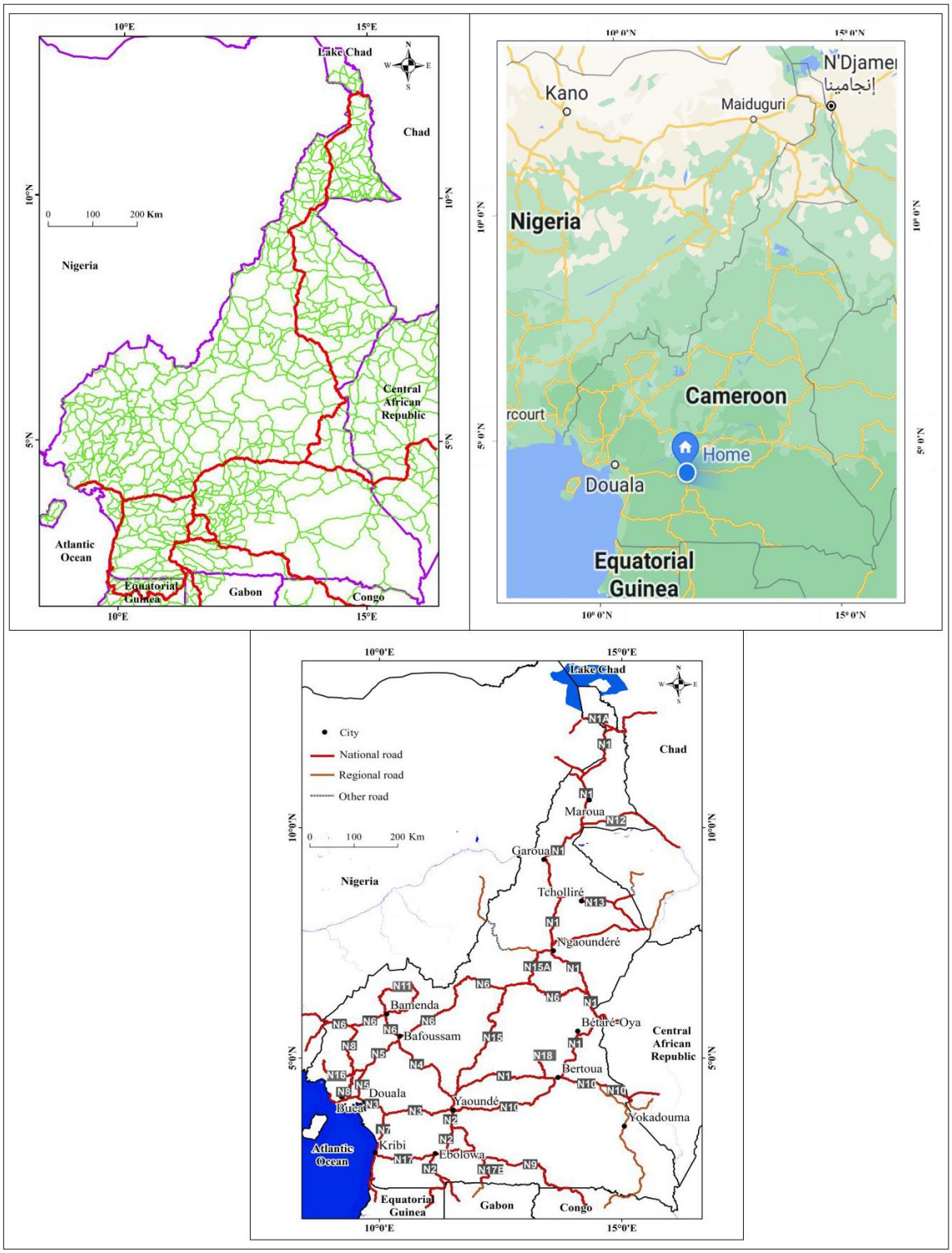


**Figure 3.** Main corridors in Central Africa (a) from [10], (b) from [58], (c) from [59].

## 3. Material and methods

### *3.1. Data*

To visualise the geological features on the Earth's surface, remote sensing methods were used for their ability to cover large areas in a short time.

 doi:10.20944/preprints202308.1946.v1



3.1.1. Landsat 8 OLI/TIRS

Although the method used is broad-spectrum, it was important to select the sharpest scenes from those acquired by the Landsat 8 satellite since its launch into orbit.

In short, 28 Landsat 8 scenes acquired have been geometrically corrected in World Geodetic System (WGS-84, Zone 32N and 33N) and converted in Universal Transverse Mercator (UTM) coordinate systems, were used for this work and are listed in Table 1. The use of these images is justified by their spectral characteristics and their spatial resolution (30m), which are suitable for structural analysis. Launched in 2013, Landsat 8 is an American Earth observation satellite. The eighth satellite in the Landsat programme and the seventh to reach orbit successfully, it comprises two sensors, including OLI and TIRS (Thermal Infrared Sensor). The OLI sensor is characterised by 9 bands, including 4 in the visible range (0.43 - 0.67µm), 1 in the near infrared range (0.85 - 0.88 µm), 2 in the mid-infrared range (1.57 - 2.29 µm), 1 band in the Cirrus range (0.50 - 0.68 µm) and 1 panchromatic band (0.50 - 0.68 µm). All bands of this sensor have a resolution of 30 m except the panchromatic band which has a resolution of 15 m. The TIRS sensor consists of two bands, all in the Thermal Infrared range (10.60 - 12.51 µm) and each with a resolution of 100 m. In this work only some of the OLI bands were used.

**Table 1.** Landsat 8 OLI/TIRS information used in this study.

| Scenes | Row | Path | Acquisition date | Level |
|---|---|---|---|---|
| 1 | 58 | 182 | 01/05/2020 | 1 |
| 2 | 59 | 182 | 01/05/2020 | 1 |
| 3 | 55 | 183 | 13/02/2020 | 1 |
| 4 | 57 | 183 | 13/02/2020 | 1 |
| 5 | 58 | 183 | 28/01/2020 | 1 |
| 6 | 51 | 184 | 20/02/2020 | 1 |
| 7 | 52 | 184 | 04/02/2020 | 1 |
| 8 | 53 | 184 | 04/02/2020 | 1 |
| 9 | 54 | 184 | 20/02/2020 | 1 |
| 10 | 55 | 184 | 20/02/2020 | 1 |
| 11 | 56 | 184 | 18/11/2020 | 1 |
| 12 | 57 | 184 | 18/11/2020 | 1 |
| 13 | 58 | 184 | 23/12/2015 | 1 |
| 14 | 51 | 185 | 27/02/2020 | 1 |
| 15 | 52 | 185 | 11/02/2020 | 1 |
| 16 | 53 | 185 | 11/02/2020 | 1 |
| 17 | 54 | 185 | 11/02/2020 | 1 |
| 18 | 55 | 185 | 11/02/2020 | 1 |
| 19 | 56 | 185 | 11/02/2020 | 1 |
| 20 | 57 | 185 | 26/01/2020 | 1 |
| 21 | 58 | 185 | 26/01/2020 | 1 |
| 22 | 55 | 186 | 18/02/2020 | 1 |
| 23 | 56 | 186 | 05/03/2020 | 1 |
| 24 | 57 | 186 | 06/01/2016 | 1 |
| 25 | 58 | 186 | 29/03/2017 | 1 |
| 26 | 55 | 187 | 25/02/2020 | 1 |
| 27 | 56 | 187 | 24/01/2020 | 1 |
| 28 | 57 | 187 | 29/01/2016 | 1 |

 doi:10.20944/preprints202308.1946.v1



3.1.2. SRTM (Shuttle Radar Topography Mission)

SRTM data of 30m resolution were also used in this work. 63 SRTM scenes covering the entire study area were used. Information on the SRTM can be found in Farr et Kobrick [60].

Both datasets used in this work were downloaded from the website https://earthexplorer.usgs.gov [61].

3.1.3. Field data

Field campaigns were carried out during the dry season from 2019 to 2023 using compasses, GPS, distance meters and altimeters to identify fault zones and areas of possible landslides [10], particularly on the N3 national road. This road was chosen as the pilot zone because it is the main road linking the port area (from the Atlantic Ocean) to all the other countries in Central Africa and belongs to both the equatorial zone and the coastal zone, characterised by a high level of cloud cover. Longitudinal and transverse faults more than 5 km long were investigated, as they have a very large lengthwise extension and are therefore difficult to modify by human activity.

*3.2. Methodology*

3.2.1. Preprocessing

In this step, after mosaicing all these scenes, radiometric processing, haze reduction and histogram equalisation were applied in order to improve the contrast of the satellite image; noise reduction was also applied, with the aim of filtering out the noise from the image. In addition, Pansharpening, which merges high resolution panchromatic and low resolution multispectral images to create a single high resolution colour image, was applied to reduce the resolution of the satellite image from 30m to 15m.

3.2.2. Processing

- Principal component analysis (PCA)

PCA is an analytical method used to compress the information contained in the original bands into new bands called principal components, by eliminating data redundancy [58–60]. It has been used in radiometric studies by several authors [62–65].

In this study, it was applied to the combination of bands 7, 6, 2.

- Directional filtering

The filtering operation consists in modifying the value of a pixel according to that of its neighbours [66–68]. The aim of this method is to highlight structural discontinuities and facilitate the discrimination of lineaments in all possible directions and to bring out the maximum number of lineaments. The filters used in this work are Sobel directional filters applied in four directions: N-S, E-W, NE-SW, SE-NW with convolution matrices of size 7×7 [11,69]. Several studies have shown the effectiveness of combining different image processing techniques to improve image contrast, thus better highlighting geological discontinuities and faults [70,71]. In this respect, PCA is applied here in combination with the Sobel filtering method. This task was carried out using ERDAS Imagine software.

- Shaded relief

Shaded relief thematic maps are a visual representation of the terrain consisting of grey values stored in raster images, derived from the Digital Elevation Model (DEM). Shaded relief is commonly used in the extraction of lineaments from the SRTM image [72]. For this purpose, some parameters have to be applied to the input SRTM data, such as changing the virtual azimuth of the sun while maintaining its elevation marker in order to create a shaded relief [73]. This will result in four shaded relief images that will be output files with an azimuth of 0°, 45°, 90° and 135°.

 doi:10.20944/preprints202308.1946.v1



This task was carried out with ArcGIS software using the spatial analyst tool hillshade.

The boundaries between shaded and unshaded areas could indicate the presence of lineaments [74].

- Manual and automatic lineament extraction

Automatic extraction was applied to the principal component of the filtered Landsat image and to the shaded relief of the SRTM image in the four preferred directions. This was done with the PCI Geomatica software via the LINE module algorithm using the optimal parameter values presented in Table 2. Similarly, manual extraction using ArcGIS software was applied to the filtered Landsat 8 principal component and SRTM shaded relief, in the four preferred directions NS, NE-SW, NW-SE and EW. The application of the different processing methods on the Landsat 8 and SRTM images led to the lineament map of the study area. The main steps that led to the extraction of the lineaments are summarised in Figure 4. Lineaments indicating either faults or fractures are considered as faults if they result in a variation in height of at least 30 m on the DEM, and fractures if they do not.

- Rose diagram

The conventional method is to produce the directional rosettes proportional to the cumulative length of the lineaments by $10^0$ orientation class [73,75,76]. This task was performed using Rockworks software.

As lineament extraction can generate many artefacts especially by automatic methods [77], any lineament corresponding to anthropogenic features was identified and removed, with the exception of linear forms similar to roads, given the purpose of the study. Lineaments digitised from the geological map, DEM and slope were also useful for validation.

**Table 2.** Values of the parameters applied for the extraction of lineaments.

| Threshold parameters and units | default values | Selected values |
|---|---|---|
| RADI (In pixels) | 10 | 10 |
| GTHR (In range, 0–255) | 100 | 80 |
| LTHR (In pixels) | 30 | 30 |
| FTHR (In pixels) | 3 | 3 |
| ATHR (In degrees) | 30 | 20 |
| DTHR (In pixels) | 20 | 20 |

- **Slope**

Derived from the DEM (Figure 5), the slope map (Figure 6) expresses the change in elevation, where high values correspond to steep slopes and low values to flat areas. High values of slope correspond to abrupt and uneven changes, and are often key indicators of the presence of lineaments [78,79]. A slope is declared a landslide zone if it is greater than $6^0$ and its height greater than 30 m, even though it is true that, for slopes less than 30 m high, we can still observe small falls of particles torn off not only from the rock, but also from the small sedimentary cover above.

 doi:10.20944/preprints202308.1946.v1



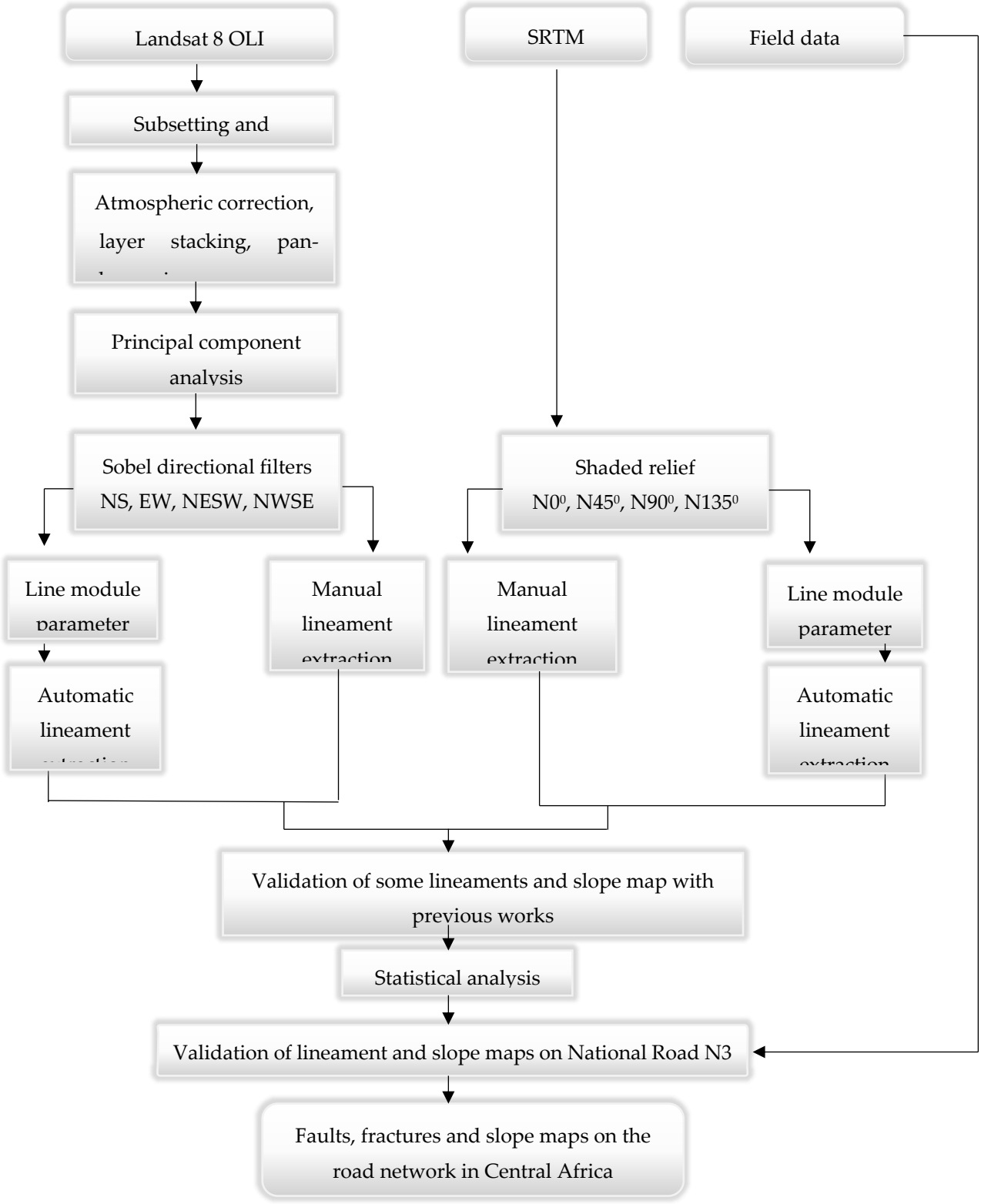


**Figure 4.** Flow chart of the methodology used in this study.

Preprints (www.preprints.org) | NOT PEER-REVIEWED | Posted: 29 August 2023 doi:10.20944/preprints202308.1946.v1



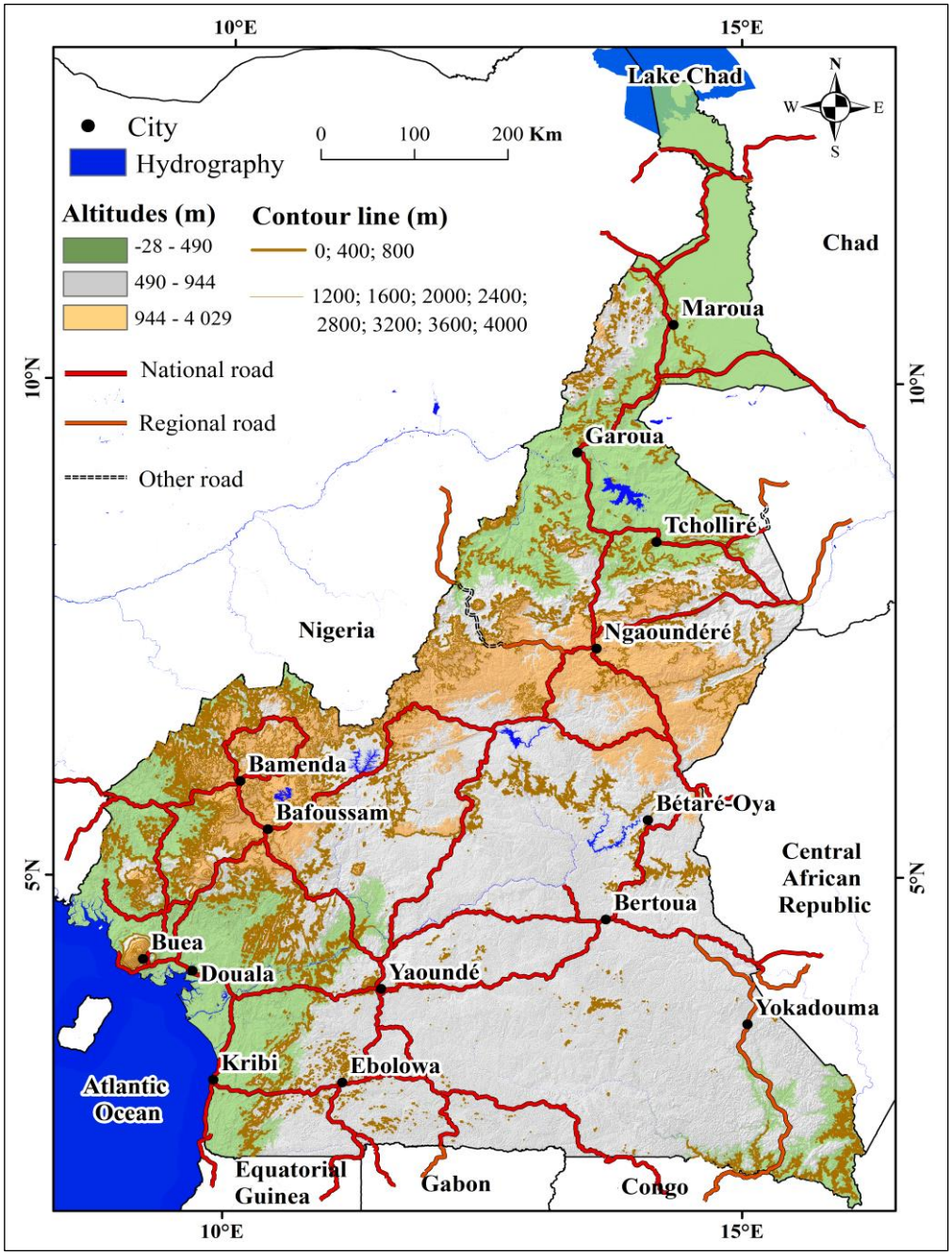


**Figure 5.** Elevation map.

## 4. Results and discussion

### *4.1. Results*

#### 4.1.1. Lineaments obtained

Both manual and automatic extraction methods were used to map the lineaments (Figure 7a). The statistical analysis of the lineaments obtained in this work shows 2321 (of which 1052 manual and 1269 automatic) and 3142 (of which 1874 manual and 1268 automatic) lineaments extracted from Landsat 8 and SRTM images respectively. In order to facilitate the comparison between the lineaments obtained and the faults of the geological map, in the following work, only lineaments of at least 5 km in length were taken into account. The lineaments obtained by the manual approach have lengths ranging from 5 to 65 km with an average length of 11 km for Landsat 8 images, while

 doi:10.20944/preprints202308.1946.v1



the lineaments extracted from SRTM images have lengths ranging from 5 to 356 km with an average length of 20 km. For the automatic extraction, the lineament lengths vary from 5 to 35 km with an average value of 6 km, and from 5 to 30 km with an average value of 6 km for Landsat 8 and SRTM images respectively. The final lineament map was generated by integrating all automatically and manually extracted lineaments for each dataset (Figure 7a); thus 5463 lineaments were identified. After removing repetitive lineaments, 5222 lineaments were retained, constituting the final lineament map; their lengths ranged from 5 to 356 km with directions N160 and N33 respectively, and a mean of 12 km and a standard deviation of 14 km (Figure 7b). Lineaments shorter than 12 km are the most numerous and constitute a percentage of 73%. The statistical analysis of the lineaments has been investigated by several authors in order to study the geometry of the lineament network and to identify the dominant directions in the area.

In this work, two types of directional rosettes were performed, the length-based rosette (Figures 7c) and the number-based rosette (Figures 7d) of the lineaments. The rose diagram obtained as a function of the length of the lineaments shows a predominance of the N20-N30, N100-N110, N30-N40 and N110-N120 direction classes. The N20-N30 direction would therefore be the main direction of deformation, and the N110-N120 direction, which is perpendicular to it, would be the direction of major stresses.

Preprints (www.preprints.org) | NOT PEER-REVIEWED | Posted: 29 August 2023 doi:10.20944/preprints202308.1946.v1



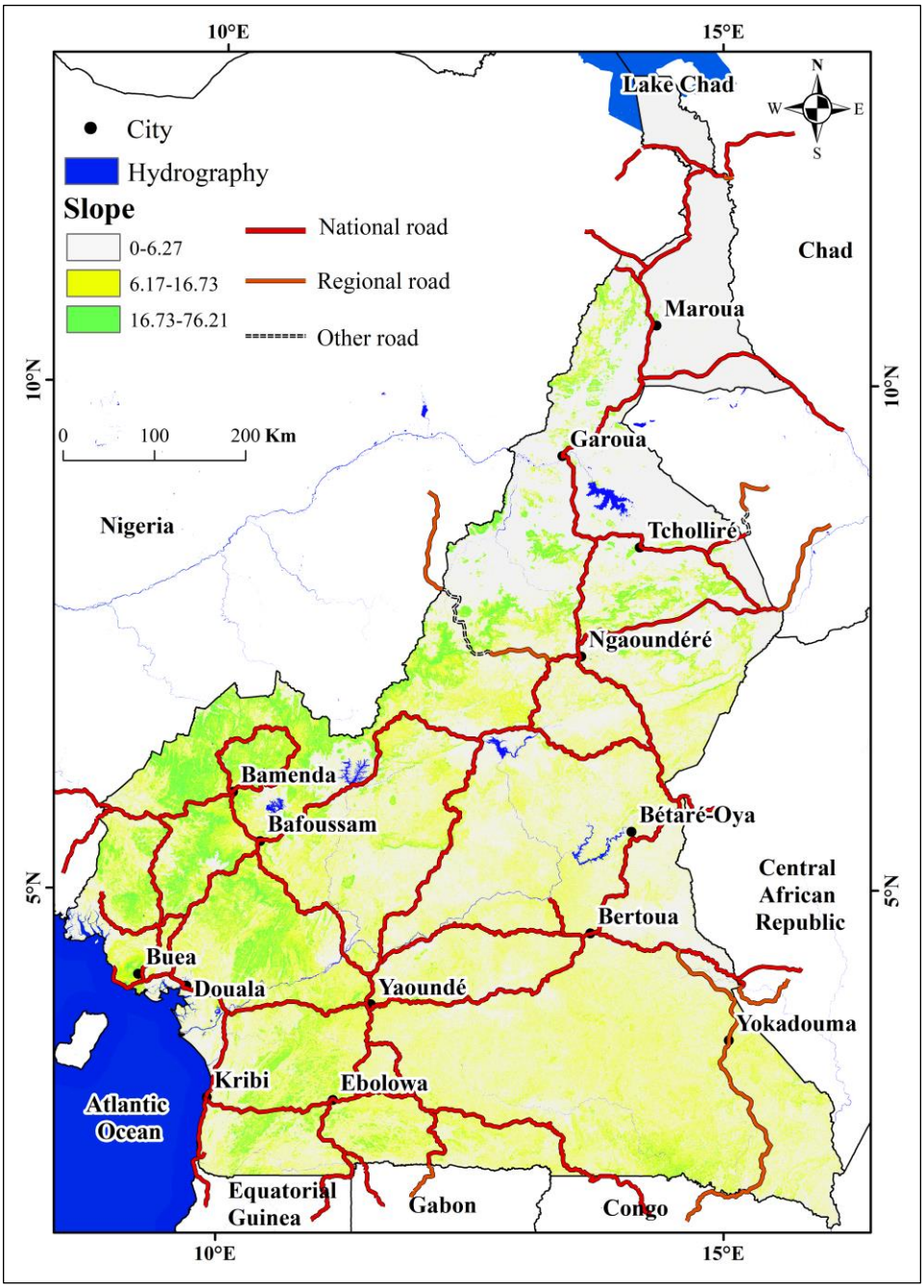


**Figure 6.** Slope map.

Preprints (www.preprints.org) | NOT PEER-REVIEWED | Posted: 29 August 2023 doi:10.20944/preprints202308.1946.v1



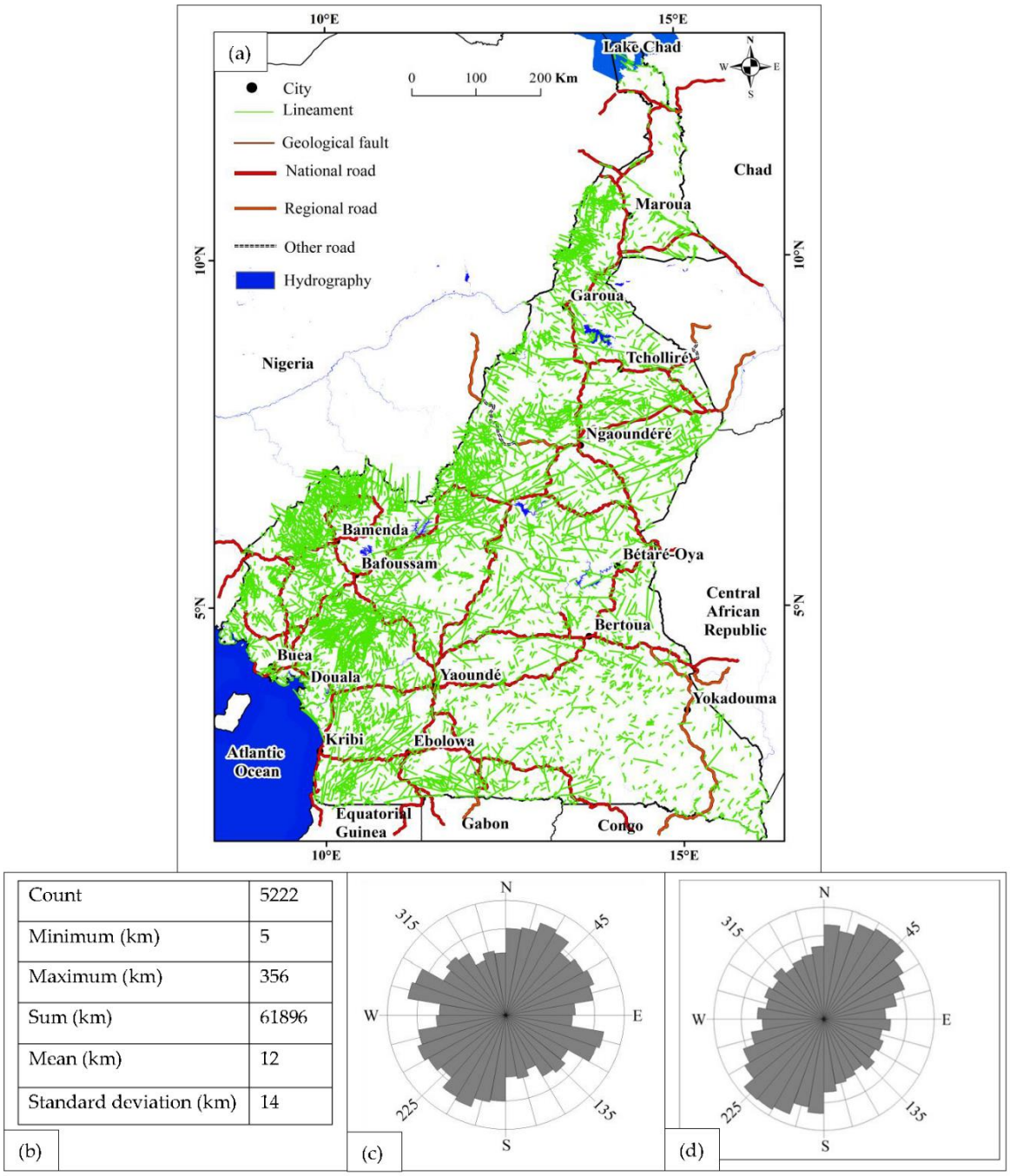


| | |
|---|---|
| Count | 5222 |
| Minimum (km) | 5 |
| Maximum (km) | 356 |
| Sum (km) | 61896 |
| Mean (km) | 12 |
| Standard deviation (km) | 14 |

**Figure 7.** (**a**) Study area lineaments; (**b**) Basic statistics associated; (**c**) Rose diagram as a function of length; (**d**) Rose diagram as a function of frequency.

### 4.1.2. Altimetry

The relief map (Figure 5) obtained from the DEM is divided into three classes, namely low altitudes ranging from 0 to 490 m in the coastal regions and the north, medium altitudes ranging from 490 to 944 m in the centre and south, and high altitudes ranging from 944 to 4029 m.

### 4.1.3. Slope

The resulting slope map has also 3 classes, low slope class ranging from 0 to 6; medium slope class ranging from 6 to 17 and high slope class ranging from 17 to 76. The high slope areas are concentrated to the west of the study area, slightly to the north and to the southwest. Areas of medium slope are found further south, east and west, and areas of low slope to the north and east.

Preprints (www.preprints.org) | NOT PEER-REVIEWED | Posted: 29 August 2023 doi:10.20944/preprints202308.1946.v1



*4.2. Discussion*

4.2.1. validation of road map

The road maps proposed by [10] (Figure 3a) and [58] (Figure 3b) have shortcomings, which has led us to propose a new map (Figure 3c), showing more details than previous ones, while at the same time bringing out 100% of the road network illustrated by the previous two maps.

**First validation of lineament map**

4.2.2. Correlation of lineaments with the geological map

Figure 8 shows the lineaments superimposed on the geological faults. Among the 20 faults of the geological map, 16 were found, which is a percentage of 80%. By overlaying, for an initial validation, the network of lineaments obtained having more than 5 km with that of the known faults, it appears 4 faults F1, F9, F17 and F18 (Figure 8) which could not be identified by the present work. Field validation of faults F1, F9, F17 and F18 was not possible due to difficult access conditions, so a new field campaign along the N3 was carried out to validate them. Table 3 shows the lineaments obtained and the geological faults to which they correspond and overlap. Figure 7 shows that the lineaments are highly concentrated along the Cameroon Volcanic Line (CVL), the Foumban Shear Zone (FSZ), the Southern Cameroon Shear Zone (SCSZ), and in the southern part of the Central Cameroon Shear Zone (CCSZ), in the northern part of the Kribi-Campo Shear Zone (KCSZ) and in the eastern part of the Congo Craton. In the far north, the concentration of lineaments is low, which would certainly be due to the presence of sand and alluvium covering the ground. Overlaying the lineaments on the geological map shows that the fracture density in the Congo Craton is 0.13 while that in the mobile zone is 0.14. This shows that the Congo Craton, which was thought to be stable, appears to be highly fractured, especially in the western and central flanks. It is understandable why earthquakes [80] are felt in the areas contained in this unit.

**Table 3.** Table showing the equivalence between the lineaments obtained and the geological faults.

| N⁰ | Lineaments | Geological faults | Corresponding road |
|---|---|---|---|
| **1** | / | F1 | / |
| 2 | L1 | F2 | N1 |
| 3 | L14 | F3 (FSZ) | N4, N6 |
| 4 | L13 | F4 | N6, N15A |
| 5 | L9, L10, L11, L12 | F5 (CCSZ) | N6, N15A |
| 6 | L16 | F6 (KCSZ) | N3, N17 |
| 7 | L15 | F7 (SCSZ) | N3, N4 |
| 8 | L8 | F8 | N6 |
| 9 | / | F9 | N15 |
| 10 | L6 | F10 | N1 |
| 11 | L7 | F11 | / |
| 12 | L5 | F12 | / |
| 13 | L4 | F13 | N13 |
| 14 | L27 | F14 | / |
| 15 | L28 | F15 | / |
| 16 | L23, L24, L25, L26 | F16 (MSZ) | N1, N6 |
| 17 | / | F17 | N1 |
| 18 | / | F18 | / |

Preprints (www.preprints.org) | NOT PEER-REVIEWED | Posted: 29 August 2023 doi:10.20944/preprints202308.1946.v1



| | | | |
|---|---|---|---|
| 19 | L2, L3 | F19 (TBSZ) | N1, N13 |
| 20 | L17, L18, L19, L20, L21, L22 | F20 (SCZ) | N3, N4, N15 |

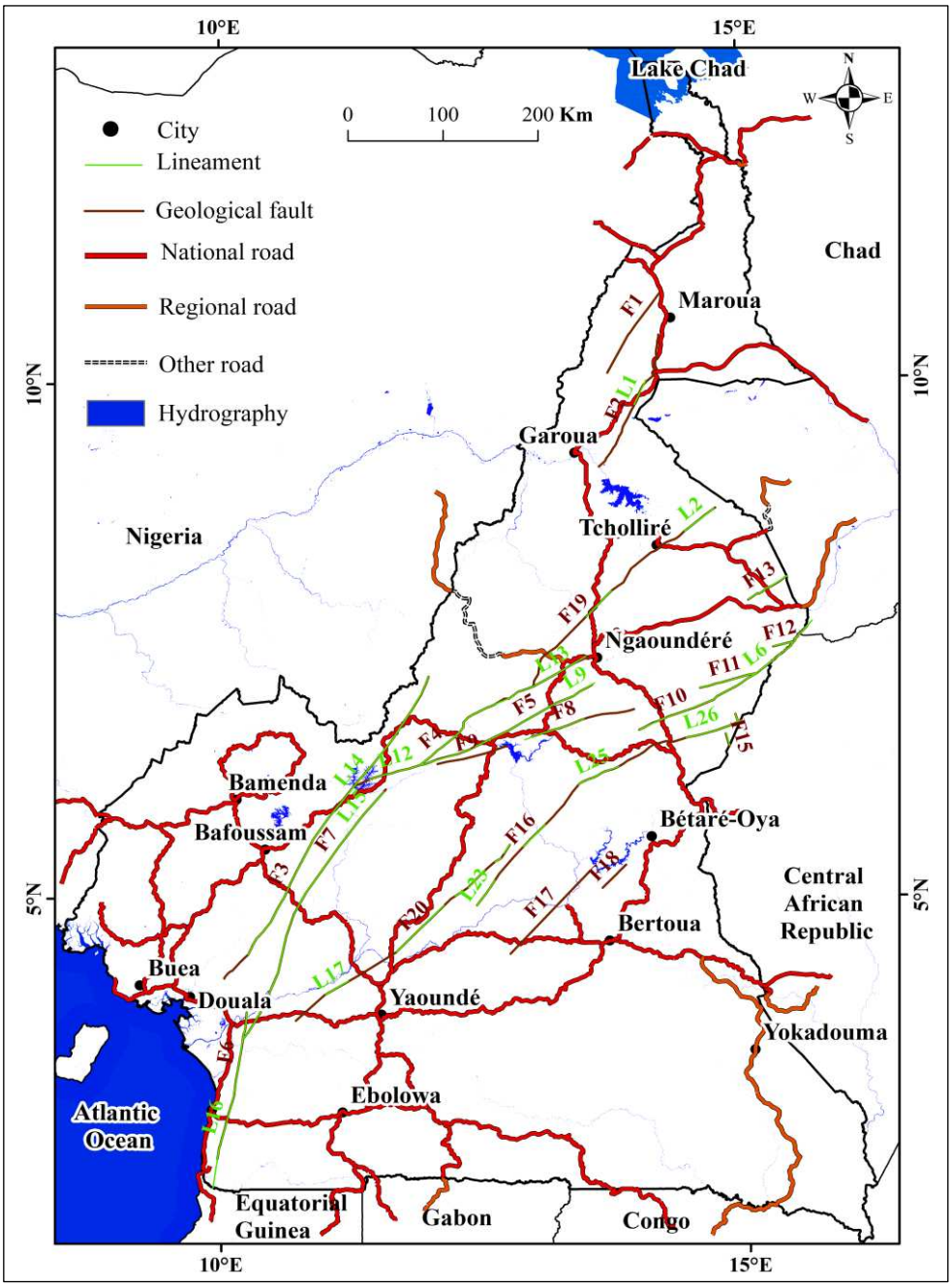


**Figure 8.** Lineaments superimposed on geological faults.

4.2.3. Correlation of the lineaments with some previous geophysical work

In addition to the geological faults found by [47], this work has highlighted the fault announced by [81] at the level of Akono-Mbalmayo but which until now has remained little known probably because of the particularly difficult access conditions. Among the faults highlighted by [8], 4 of the 5 confirmed faults and 7 of the 8 assumed faults were found. Only 3 of the confirmed faults intercept the main road network. In addition, the lineaments show a strong concentration around Lakes Nyos and Manengouba, as observed by [11,82].

Likewise, the directional rosette obtained as a function of the greatest number of lineaments showed a predominance of the N40-N50, N30-N40, N20-N30 and N0-N10 direction classes (Figure

 doi:10.20944/preprints202308.1946.v1



7d). The N40-N50 direction was found in the work of [8], relating to the occurrences of fault and landslide in the West Cameroon region, identifying the N45-N50 direction as the predominant orientation of lineaments.

Similarly, the study carried out by [83], on mapping of major tectonic lineaments across Cameroon also revealed that lineaments are mainly oriented in the N45 direction. The N0-N10 direction obtained in this work was also identified by [83]. The N20-N30 direction was highlighted in the work of [11], on fracture comparison models in CVL, where the N20 and N30 directions were obtained for Landsat 8 and Landsat 7 images respectively.

4.2.4. Correlation of the lineaments with the elevation map

The correlations between Figure 7a and Figure 5 show a relief demarcation observed between Kribi and Ebolowa corresponding to the Kribi-Campo Shear Zone (KCSZ) fault family found in Figure 2 and Figure 7a. Between Bafoussam and Bertoua, the combination of Figures 7a and 5 also shows a fault family in the Foumban Shear Zone (FSZ) and that the cliffs of Dschang and Ngaoundéré lie in zones of high elevation and high fracture density. Furthermore, the correlation between Figure 7a and Figure 5 shows that, of the 373 lineaments obtained, 255 are fractures, 115 are normal faults and 3 are fractures in one of their portions and normal faults in their extension. The lineaments categorised as fractures in Figure 8 can lead to cracks along the road like those observed in Figures 1c, 1e and those categorised as normal faults can lead to subsidence and block collapse (Figure 1f).

**Second validation of lineament map**

Field investigations for N3 showed that all faults and fractures (Table 4) with a longitudinal extension greater than 5 km in both coastal and forest zones (for the 28 scenes used with cloud percentages of 0%, 0.31%, 3.24%, 6.02% and 46%) can be mapped using the method described in the flow chart (Figure 4).

Similarly, a fault found on the map from satellite data may correspond to several fault systems, as in zones FZ5N3, FZ6N3, FZ7N3 and FZ8N3 (Figure 9, Table 4). The 03 faults F11N3, F12N3 and F13N3 (Figure 9) described in the geological documents [11] and mapped in this study were confirmed by the field work, as were the 26 other new faults. In addition, the zones of fractures (20) and slopes (18) highlighted in the course of this work and not all observable in the existing geological documents were also validated by this study. However, the accuracy of the location of fault zones varied from 0 to 100 m. In addition, the approach used in this work made it possible to map all the areas around which landslides may occur. But unlike the location of fault zones, the deviation in the location of landslide zones varied from 0 to 500 m on average in relation to the road. The 4 faults F1, F9, F17 and F18 not found previously could be due to the fact that their difference in height is less than 30 m (which corresponds to the resolution of the DEM used), or else they could be contacts between different geological formations, covered by a sedimentary layer. All these results show that the use of Landsat 8 and SRTM data can be effective for the sustainable layout of roads and motorways in Central Africa and throughout the world, while making a relevant contribution to reduce the cost of their construction, which is still very high in Central Africa (between 336,944 $ to 4,930,885 $ [1–4]).

Preprints (www.preprints.org) | NOT PEER-REVIEWED | Posted: 29 August 2023 doi:10.20944/preprints202308.1946.v1



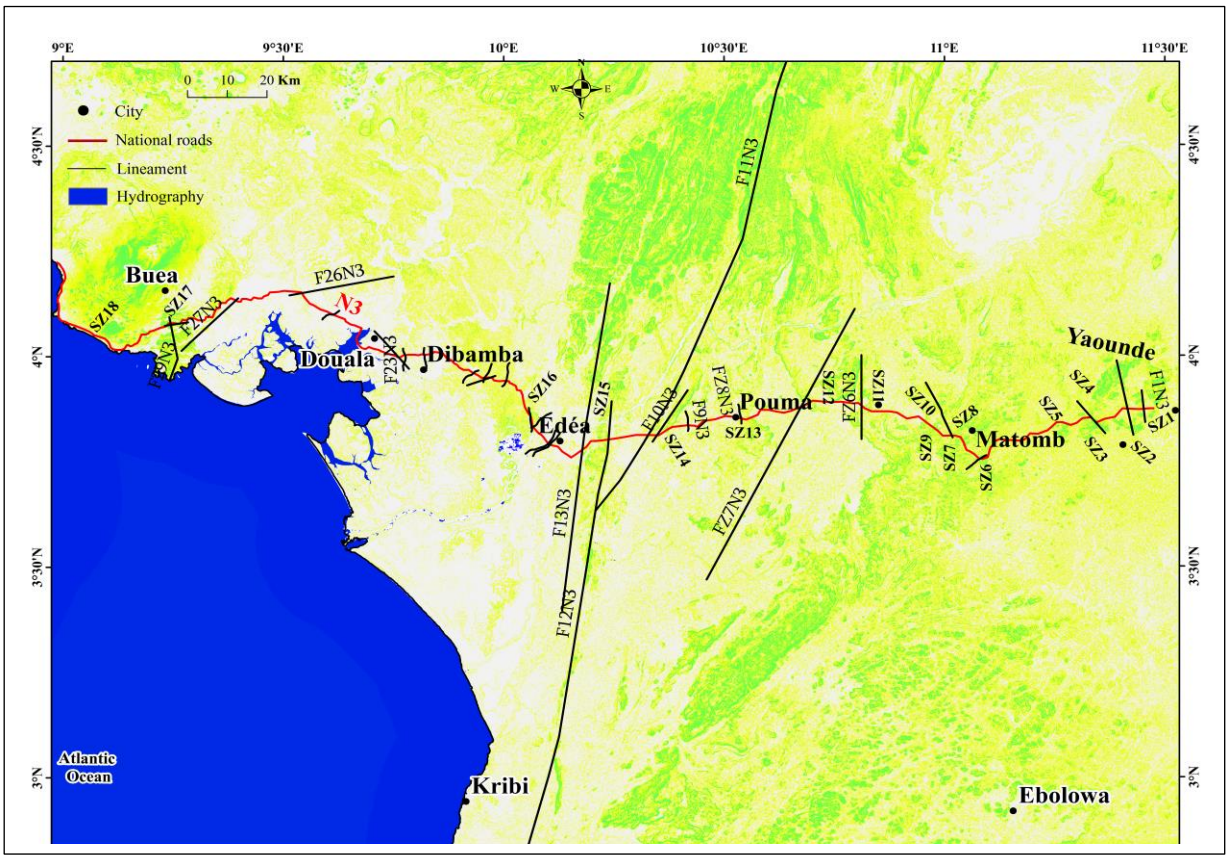


**Figure 9.** Faults, fractures and slopes around the N3 road.

**Table 4.** Coordinates of the various faults, fractures and slopes along the N3 national road.

| | Lineament | | | Slope | |
|---|---|---|---|---|---|
| F1N3 | 11°26'55,5"E | 3°52'30,8"N | SZ1 | 11°28'16,2"E | 3°52'6,6"N |
| F2N3 | 11°24'40,7"E | 3°52'45,"N | SZ2 | 11°22'53,7"E | 3°51'0,5"N |
| F3N3 | 11°19'59,3"E | 3°51'0,2"N | SZ3 | 11°19'11,5"E | 3°50'58,3"N |
| F4N3 | 11°4'39,4"E | 3°45'18,1"N | SZ4 | 11°20'34,7"E | 3°50'30,2"N |
| FZ5N3 | 11°0'53,6"E | 3°48'38,4"N | SZ5 | 11°16'30,2"E | 3°50'8,5"N |
| FZ6N3 | 10°48'35,6"E | 3°52'57,3"N | SZ6 | 11°2'39,1"E | 3°47'23,2"N |
| FZ7N3 | 10°40'24"E | 3°52'51,4"N | SZ7 | 11°2'35,8"E | 3°47'15"N |
| FZ8N3 | 10°32'12,1"E | 3°51'22,8"N | SZ8 | 11°2'3,1"E | 3°48'24,7"N |
| F9N3 | 10°20'45,7"E | 3°48'45,4"N | SZ9 | 10°57'14,4"E | 3°50'36,5"N |
| F10N3 | 10°24'59,7"E | 3°50'16,9"N | SZ10 | 10°58'26,5"E | 3°49'43,3"N |
| F11N3 | 10°19'41,7"E | 3°48'54,7"N | SZ11 | 10°49'37"E | 3°52'15,1"N |
| F12N3 | 10°14'14,6"E | 3°48'9,3"N | SZ12 | 10°44'52,8"E | 3°53'28,4"N |
| F13N3 | 10°10'39,5"E | 3°46'42,3"N | SZ13 | 10°33'41"E | 3°51'11"N |
| F14N3 | 10°6'16,5"E | 3°47'24"N | SZ114 | 10°22'25,3"E | 3°49'37"N |
| F15N3 | 10°5'58,2"E | 3°47'35,5"N | SZ15 | 10°12'60"E | 3°48'5,1"N |
| F16N3 | 10°3'59,5"E | 3°49'55,8"N | SZ16 | 10°3'38,4"E | 3°51'31,5"N |
| F17N3 | 10°3'29,9"E | 3°51'30"N | SZ17 | 9°14'17,9"E | 4°4'36,7"N |
| F18N3 | 10°0'18,1"E | 3°56'26,6"N | SZ18 | 9°11'14,3"E | 4°3'15,8"N |

| | | |
|---|---|---|
| F19N3 | 9⁰58'10"E | 3⁰57'1,2"N |
| F20N3 | 9⁰57'22"E | 3⁰56'59"N |
| F21N3 | 9⁰55'50,5"E | 3⁰57'40,5"N |
| F22N3 | 9⁰49'8"E | 4⁰0'19,4"N |
| F23N3 | 9⁰46'32,4"E | 4⁰0'12,7"N |
| F24N3 | 9⁰45'42"E | 3⁰59'52,1"N |
| F25N3 | 9⁰36'37,8"E | 4⁰6'0,2"N |
| F26N3 | 9⁰32'28,5"E | 4⁰9'4,2"N |
| F27N3 | 9⁰23'32,9"E | 4⁰7'55,5"N |
| F28N3 | 9⁰14'12,2"E | 4⁰4'26,7"N |
| F29N3 | 9⁰14'39,6"E | 4⁰4'45"N |

4.2.5. Correlation of lineaments with the slope map

By overlaying Figure 7a and Figure 6, we observe a strong concentration of lineaments that correlate with areas of steep slopes showing that roads can be subject to numerous rockfall phenomena. Thus, Figure 6 allows to understand and justify the landslides on the national roads N1, N4, N5, N6, at the level of some localities [8,84,85].

4.2.6. Correlation of the slope map with the geological map

Correlating Figures 2 and 6, it can be observed that the road sections N1, N2, N3, N4, N6, N7, N10, N11, N12, N13, N15, N15A located on gneissic formations could be prone to slope failures if they have slopes greater than $10^0$ according to the work of [10] (Figure 10). In addition, the sections of national roads N1, N3, N5, N6, N7, N12, N16 located on sandstone and clay formations could experience slope failures if they are located on slopes greater than $6.17^0$ according to [9].

Preprints (www.preprints.org) | NOT PEER-REVIEWED | Posted: 29 August 2023 doi:10.20944/preprints202308.1946.v1



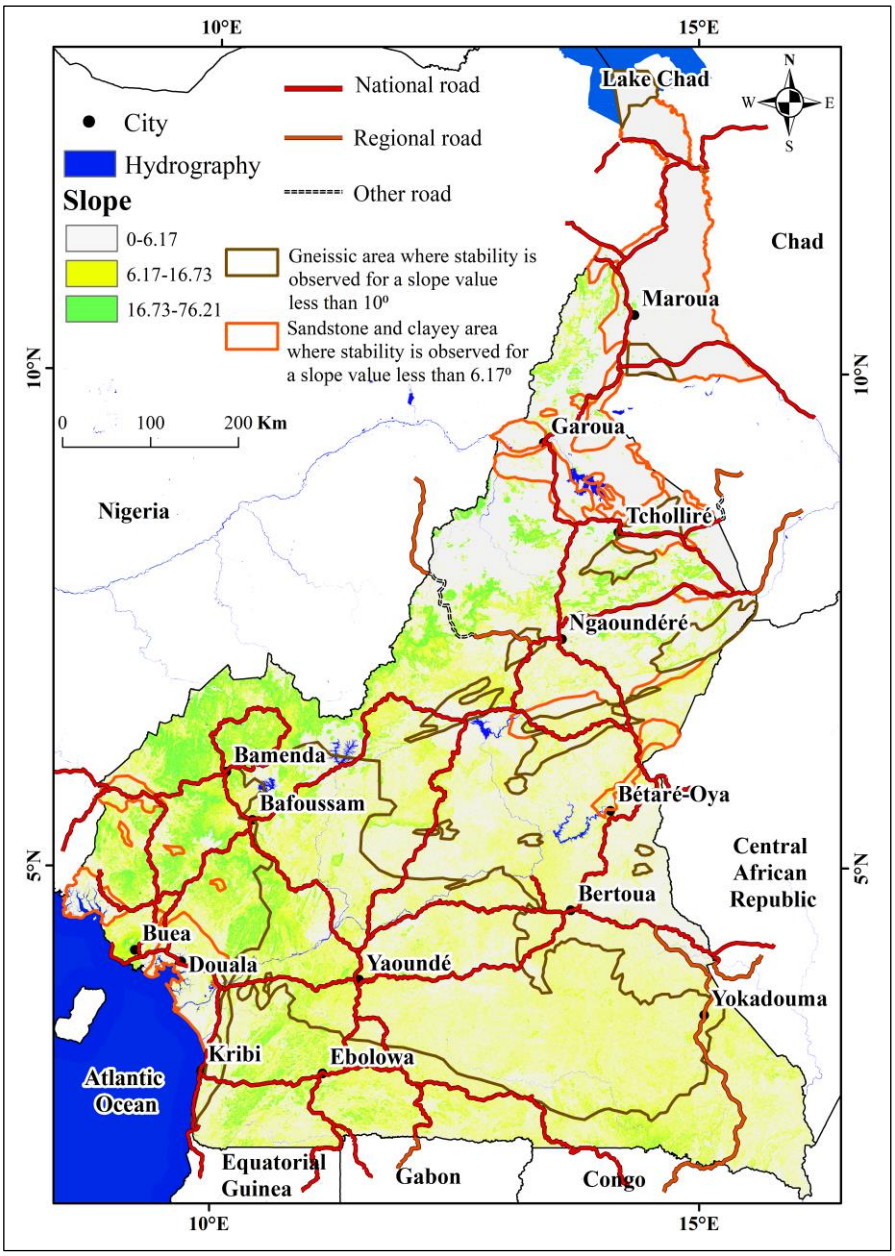


**Figure 10.** Map of the main unstable slope zones around roads and highways in Central Africa.

4.2.7. Correlation of the slope map with the road network

The Figure 6 shows that in several places on N2, N4, N5, N6, N8, N16, and N17 there may be a tendency to observe slope failures as was the case of [84]. These particle falls are particularly heavy on the N6 road linking Cameroon to Nigeria, in a NW-SE and NE-SW direction.

4.2.8. Correlation of lineaments with the road network

The superposition of Figure 3 and Figure 7a shows that 373 fault and fracture lineaments intercept the road network from north to south and from east to west (Figure 11a), showing that tectonic activity can have consequences on the road network, unlike the geological map, where only 14 faults intercept the road network (Figure 2), hence the validity of the study.

Preprints (www.preprints.org) | NOT PEER-REVIEWED | Posted: 29 August 2023 doi:10.20944/preprints202308.1946.v1



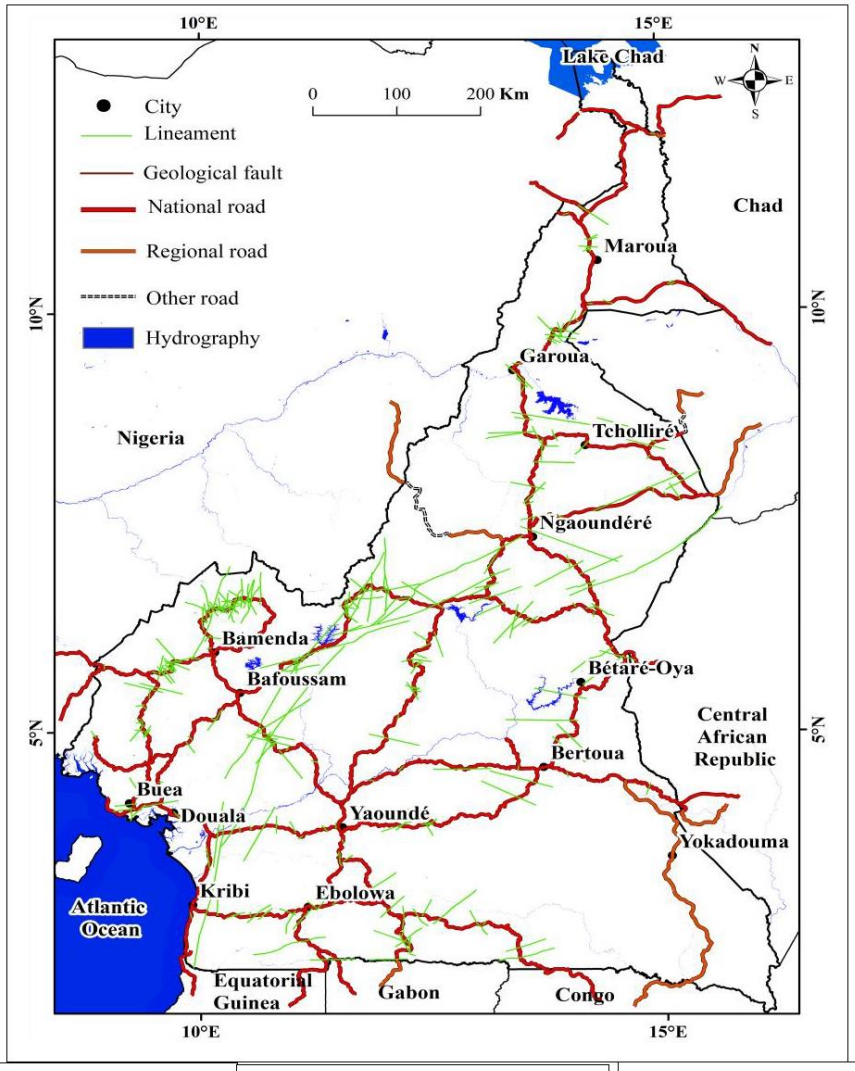


| | |
|---|---|
| Count | 373 |
| Minimum (km) | 5 |
| Maximum (km) | 356 |
| Sum (km) | 10292 |
| Mean (km) | 28 |
| Standard deviation (km) | 38 |

(b)

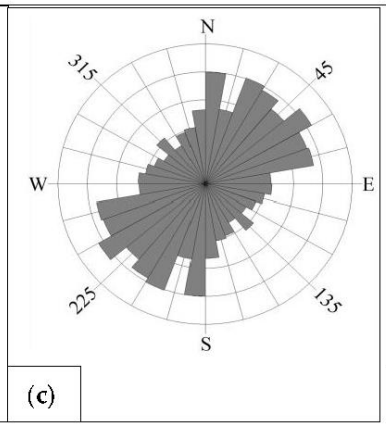


(c)

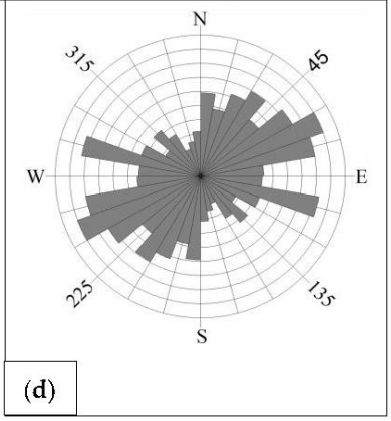


(d)

**Figure 11.** (**a**) Faults and fractures zones intersecting the road and highway network in Central Africa; (**b**) Basic statistics associated; (**c**) Rose diagram as a function of frequency; (**d**) Rose diagram as a function of length.

Their lengths vary from 5 to 356 km with an average of 28 km and a standard deviation of 38 km (Figure 11b), indicating a wide dispersion of lengths. The rose diagrams plotted against the frequency (Figure 11c) and length (Figure 11d) of the lineaments shows that the lineaments interfering with the road network are predominantly oriented in the N60-N70 and N50-N60 directions respectively. Among these lineaments, 18 run along the road network, 2 overlap and 2 intercept. The results obtained show that there are not only 14 faults (Figure 2) intercepting the road network, but that there

Preprints (www.preprints.org) | NOT PEER-REVIEWED | Posted: 29 August 2023 doi:10.20944/preprints202308.1946.v1



are still others that have created and could create shears and collapses on the road network, as shown in Table 5.

**Table 5.** Types of accident that may occur on the roads studied.

| N⁰ | Road Name | Accident type | | | | |
|---|---|---|---|---|---|---|
| | | Zone of possible landslides | Possible collapse zone | | Possible shear zone | |
| | | | Transverse | Longitudinal | Transverse | Longitudinal |
| 1 | N1 | 5 | 7 | 0 | 65 | 7 |
| 2 | N1A | 0 | 0 | 0 | 0 | 0 |
| 3 | N2 | 4 | 4 | 1 | 4 | 1 |
| 4 | N2A | 0 | 0 | 0 | 1 | 0 |
| 5 | N3 | 18 | 8 | 1 | 19 | 1 |
| 6 | N4 | 7 | 4 | 0 | 17 | 1 |
| 7 | N5 | 4 | 8 | 0 | 6 | 0 |
| 8 | N6 | 7 | 23 | 0 | 56 | 1 |
| 9 | N6A | 1 | 0 | 0 | 1 | 0 |
| 10 | N7 | 0 | 0 | 0 | 4 | 1 |
| 11 | N8 | 4 | 7 | 0 | 13 | 1 |
| 12 | N9 | 1 | 7 | 0 | 10 | 0 |
| 13 | N10 | 3 | 4 | 0 | 9 | 0 |
| 14 | N11 | 19 | 17 | 0 | 25 | 0 |
| 15 | N12 | 0 | 0 | 0 | 8 | 1 |
| 16 | N13 | 5 | 1 | 0 | 6 | 0 |
| 17 | N13A | 1 | 0 | 0 | 3 | 0 |
| 18 | N14 | 1 | 0 | 0 | 1 | 0 |
| 19 | N15 | 4 | 10 | 0 | 8 | 0 |
| 20 | N15A | 4 | 1 | 0 | 7 | 1 |
| 21 | N16 | 7 | 1 | 0 | 3 | 0 |
| 22 | N17 | 13 | 8 | 0 | 2 | 0 |
| 23 | N17A | 3 | 1 | 0 | 0 | 0 |
| 24 | N17B | 2 | 5 | 0 | 2 | 0 |
| 25 | N18 | 0 | 1 | 0 | 1 | 0 |
| Total | | 113 | 117 | 2 | 271 | 15 |

Compared with the geological map (Figure 2), this new lineaments map (Figure 7) makes it easier to predict accidents linked to tectonic activity on the road network. The statistical analysis made it possible to obtain a correlation coefficient of 0.071, thus testifying to the existence of a correlation between the road network and the lineaments in the study area. It can thus be observed for the lineaments intercepting the road network, accidents such as the road shear, as well as a transverse subsidence of one of the two blocks on either side of the lineament (as in the Figures 1d,

1f). Lineaments overlayed on the road network are likely to cause cracks in the road and longitudinal subsidence of one of the blocks on either side of the lineament (Figures 1c, 1e). Lineaments along the road network can create accidents similar to those intercepting it. Table 5 shows that the road network in Central Africa may be subject to 113 zones of possible rockfall or landslide, 117 of possible transverse collapse zones, 2 of possible longitudinal collapse zones, 271 zones of possible transverse shear and 15 of possible longitudinal shear [8].

## 5. Conclusion

This work studies the impact of geodynamic activity on road corridors in Central Africa, with a view to monitor the present road network in a sustainable manner while planning a better route for future corridors.

To achieve this, 28 scenes with cloud percentages of 0%, 0.31%, 3.24%, 6.02% and 46% of Landsat 8 OLI, and SRTM, coupled with field data, were used. Various image processing techniques were then applied to highlight the linear structures. These included PCA, spatial filters and shaded relief, all of which proved effective in detecting and extracting lineaments. The result of the road map shows 29 main roads and 6 secondary roads. While the lineament map shows 5222 lineaments with increased fracturing densities along the Cameroon Volcanic Line, around the FSZ, CCSZ, SCSZ, Dschang and Ngaoundéré cliffs and some crater lakes; the longest following the N20-N30 orientation and the most numerous following the N40-N50. Among the linear structures identified, 376 interfere with the road network, of which 256 are fractures, 117 correspond to normal faults and 3 to fractures in one of their portions and normal faults in their extension. These results are useful for sustainable planning, management, monitoring and extension of roads worldwide, but especially in Central Africa where the road problem is still high due to the lack of large-scale information at the time of their design and construction.

**Author Contributions:** Conceptualization, P.N.N.; E.M.D.; S.C.T. and E.F.K.P.; Methodology, E.M.D.; S.C.T.; E.F.K.P.; B.P.G.P.; Software, S.C.T.; M.M.A.G.; I.M.N. and A.M.P.N.; Formal analysis, S.C.T.; B.P.G.P.; M.M.A.G.; Y.P.K.; and I.M.N.; Resources, E.M.D.; P.N.N.; S.C.T.; E.F.K.P.; B.P.G.P.; Y.P.K.; Data curation, S.C.T.; M.M.A.G.; I.M.N. and A.M.P.N.; Writing—original draft, S.C.T. and P.N.N.; Writing—review & editing, S.C.T.; Y.P.K.; B.P.G.P. and A.M.P.N.; Supervision, P.N.N. and E.M.D.; Funding acquisition, - All authors have read and agreed to the published version of the manuscript.

**Funding:** This research received no external funding.

**Data Availability Statement:** All data is included in this article

**Acknowledgments:** The authors would like to thank Dr. Blaise Pascal Ngounou Pokam, Dr. Euloge Felix Kayo Pokam, The Minister for Scientific Research and Innovation Dr. Madeleine Tchuinte, the late Nouck Mbom Jeannot and the late Ngo Matip Julienne for their support.

**Conflicts of Interest:** The authors declare no conflict of interest.

## Abbreviation

FZ : fault zone
SZ : slope zone

## References

1. Coûts unitaires des projets d'infrastructure en Afrique subsaharienne. 2008. Available online: https://www.eu-africa-infrastructure-tf.net/attachments/library/aicd-background-paper-11-unit-costs-summary-fr.pdf (accessed on 24 May 2023)
2. Coût de la route au kilomètre : Le Gabon affole les statistiques. 2016. Available online : http://news.alibreville.com/h/55354.html (accessed on 24 May 2023)

3. Gabon : Entre 1 et 3 milliards de francs CFA, le km de route le plus cher d'Afrique. 2021. Available online : https://www.gabonreview.com/gabon-entre-1-et-3-milliards-de-francs-cfa-le-km-de-route-le-plus-cher-dafrique/(accessed on 22 May 2023)
4. Le coût du km de route bitumée au Cameroun est le double du prix moyen en Afrique. 2013. Available online : https://www.investiraucameroun.com/btp/1709-4597-le-cout-du-km-de-route-bitumee-au-cameroun-est-le-double-du-prix-moyen-en-afrique (accessed on 24 May 2023)
5. Lin, Y.; Zong, Z.; Lin, J.; Li, Y; Chen, Y. Across-fault ground motions and their effects on some bridges in the 1999 Chi-Chi earthquake. Advances in Bridge Engineering 2021, 2, 8. https://doi.org/10.1186/s43251-020-00028-1
6. Cheng, R.; Hou, L.; Xu, S. A Review of Digital Twin Applications in Civil and Infrastructure Emergency Management. Buildings 2023, 13, 1143. https://doi.org/10.3390/buildings13051143
7. Carrión-Mero, P.; Briones-Bitar, J.; Morante-Carballo, F.; Stay-Coello, D.; Blanco-Torrens, R.; Berrezueta, E. Evaluation of Slope Stability in an Urban Area as a Basis for Territorial Planning: A Case Study. Appl. Sci. 2021, 11, 5013. https://doi.org/10.3390/app11115013.
8. Aretouyap, Z.; Kemgang, F. E. G.; Domra, J. K., Bisso; D.; Njandjock, P. N. Understanding the occurrences of fault and landslide in the region of West-Cameroon using remote sensing and GIS techniques. Natural Hazards 2021, 109, 1589–1602. https://doi.org/10.1007/s11069-021-04890-8
9. Biswas, R. N.; Islam, M.; Islam, M. N. Modeling on management strategies of slope stability and susceptibility to landslides catastrophe at hilly region in Bangladesh. Modeling Earth Systems and Environment 2017, 3, 977-998. https://doi.org/10.1007/s40808-017-0346-4
10. Mbouombouo, I. N.; Meli'i, J. L.; Gweth, M. M. A.; Pokam, B. P. G.; Koffi, Y. P., Njock, M. C.; Nkoma, M. A. P.; Nouck, P. N. Analysis of safety factors for roads slopes in central Africa. Engineering Failure Analysis 2022, 138, 106359. https://doi.org/10.1016/j.engfailanal.2022.106359
11. Gweth, M. M. A.; Nkoungou, H. E.; Meli'i, J. L.; Gouet, D. H.; Nouck, P. N. Fractures models comparison using GIS data around crater lakes in Cameroon volcanic line environment. The Egyptian Journal of Remote Sensing and Space Science 2021a, 24, 419-429. https://doi.org/10.1016/j.ejrs.2020.12.007
12. Nguemhe Fils, S. C.; Mongo, C. H. B.; Nkouathio, D. G.; Mimba, M. E.; Etouna, J.; Nouck, P. N.; Nyeck, B. Radarsat-1 image processing for regional-scale geological mapping with mining vocation under dense vegetation and equatorial climate environment, Southwestern Cameroon. The Egyptian Journal of Remote Sensing and Space Science 2018, 21, S43-S54. https://doi.org/10:1016/j.ejrs.2018.05.005
13. Anbalagan, R.; Singh, B. Landslide hazard and risk assessment mapping of mountainous terrains—a case study from Kumaun Himalaya, India. Engineering Geology 1996, 43, 237-246. https://doi.org/10.1016/S0013-7952(96)00033-6
14. Vu, M.-N.; Vu, M.-N.; Pham, D.-T.; Nguyen-Sy, T.; Nguyen, Q.-B.; Dang, V.-D. A Multi-Layer Blowout Model for the Tunneling Face Stability Analysis. Buildings 2023, 13, 1362. https://doi.org/10.3390/buildings13061362
15. Nagarajan, R.; RoY, A.; Kumar, R. V.; Mukherjee, A.; KhirE, M. Landslide hazard susceptibility mapping based on terrain and climatic factors for tropical monsoon regions. Bulletin of Engineering Geology and the Environment 2000, 58, 275-287. https://doi.org/10.1007/s100649900032
16. Temesgen, B.; Mohammed, M.; Korme, T. Natural hazard assessment using GIS and remote sensing methods, with particular reference to the landslides in the Wondogenet area, Ethiopia. Physics and Chemistry of the Earth, Part C: Solar, Terrestrial & Planetary Science 2001, 26, 665-675. https://doi.org/10.1016/S1464-1917(01)00065-4

17. Saha, A.; Gupta, R.; Arora, M. GIS-based landslide hazard zonation in the Bhagirathi(Ganga) valley, Himalayas. International journal of remote sensing 2002, 23, 357-369. https://doi.org/10.1080/01431160010014260
18. Lin, M.L.; Tung, C.C. A GIS-based potential analysis of the landslides induced by the Chi-Chi earthquake. Engineering Geology 2004, 71, 63-77. https://doi.org/10.1016/S0013-7952(03)00126-1
19. Soesilo, I.; Hoppin, R. Evaluation of digitally processed Landsat imagery and SIR-A imagery for geological analysis of West Java region, Indonesia. Remote sensing for ressources development and environmental management. International symposium 1986, 7, 173-182.
20. Mathew, J.; Jha, V.K.; Rawat, G.S. Application of binary logistic regression analysis and its validation for landslide susceptibility mapping in part of Garhwal Himalaya, India. Int. J. Remote Sens. 2007, 28, 2257–2275.
21. Lee, S.; Lee, M.J. Detecting landslide location using KOMPSAT 1 and its application to landslide-susceptibility mapping at the Gangneung area, Korea. Advances in Space Research 2006, 38, 2261-2271. https://doi.org/10.1016/j.asr.2006.03.036
22. Abdullah, A.; Akhir, J. M.; Abdullah, I. Automatic mapping of lineaments using shaded relief images derived from digital elevation model (DEMs) in the Maran–Sungi Lembing area, Malaysia. Electronic Journal of Geotechnical Engineering 2010, 15, 949-958.
23. Hubbard, B.M; Thompson, T.J. Lineament Analysis of Mineral Areas of Interest in Afghanistan: Automatically delineated lineaments using 30-m TM imagery. 2012. Available online :https://pubs.usgs.gov/of/2012/1048/pdf/ofr2012-1048.pdf (accessed on 21 May 2023)
24. Thannoun, R. G. Automatic extraction and geospatial analysis of lineaments and their tectonic significance in some areas of Northern Iraq using remote sensing techniques and GIS. International Journal of Enhanced Research In Science Technology & Engineering Bulletin 2013, 2, 1-11.
25. Ramli, M.; Yusof, N.; Yusoff, M.; Juahir, H.; Shafri, H. Lineament mapping and its application in landslide hazard assessment: a review. Bulletin of engineering Geology and the Environment 2010, 69, 215-233. https://doi.org/10.1007/s10064-009-0255-5
26. Al-Dossary, S.; Marfurt, K. J. Lineament-preserving filtering. Geophysics 2007, 72, P1-P8.
27. Rouse, J.; Haas, R.; Schell, J.; Deering, D. Monitoring vegetation systems in the great plains with ERTS Third ERTS Symposium (pp. 309–317). Washington, DC: NASA. 1973. Available online: https://ntrs.nasa.gov/api/citations/19740022614/downloads/19740022614.pdf (accessed on 7 February 2023)
28. Gazel, J.; Guiraudie, C. Notice Explicative sur la Région Abong-Mbang Ouest de la Carte Géologique de Reconnaissance à l'échelle du 1/500.000. 1965. Direction des Mines et Géologie, Yaoundé, 29 p. Avaiable online :https://books.google.com/books/about/Notice_explicative_sur_la_feuille_Abong.html?id=kaAPswEACAAJ (accessed on 2 May 2023)
29. Vicat J.-P. ; Pouclet, A. ; Nsifa E. Les dolérites du groupe du Ntem (Sud Cameroun) et des régions voisines (Centrafrique, Gabon, Congo, Bas Zaïre) : Caractéristiques géochimiques et place dans l'évolution du craton du Congo au Protérozoïque. 1998. In: J. P. Vicat, and P. Bilong, Eds., Géologie et environnements au Cameroun. Collection GEOCAM: 305-324. Avaiable online :https://www.researchgate.net/profile/Jean_Paul_Vicat/publication/281612596_Les-dolerites-du-complexe-du-Ntem-Sud-Cameroun-comparaison-avec-les-dolerites-du-Nord-Ouest-du-craton-du-

Congo-et-evolution-geodynamique-du-Paleoproterozoique-et-du-Neoproterozoique.pdf (accessed on 23 May 2023)

30. Gong, P., Yu, L., Li, C., Wang, J., Liang, L., Li, X., Ji, L., Bai, Y., Cheng, Y., Zhu, Z. A new research paradigm for global land cover mapping. Annals of GIS 2016, 22, 87-102. http:// doi.org/10.1080/19475683.2016.1164247.
31. Shrestha, D. P., Saepuloh, A., Meer, F. V. D. Land cover classification in the tropics, solving the problem of cloud covered areas using topographic parameters. International Journal of Applied Earth Observation and Geoinformation 2018, 77, 84-93. http://doi.org/10.1016/j.jag.2018.12.010.
32. Toteu, S.F.; Van Schmus, W.R.; Penaye, J.; Nyobe, J.B. U/Pb and Sm/ Nd edvidence for Eburnian and Pan-African high-grade metamorphism in cratonic rocks of southern Cameroon. Precambrian Res. 1994, 67, 321–347. https:// doi. org/ 10. 1016/ 0301- 9268(94) 90014-0.
33. Tchameni, R.; Pouclet, A.; Penaye, J.; Ganwa, A.A.; Toteu, S.F. Petrography and geochemistry of the Ngaoundere Pan-African granitoids in Central North Cameroon: Implications for their sources and geological setting. J. Afr. Earth. Sci. 2006, 44, 511–529. https://doi.org/10.1016/j.jafrearsci.2005.11. 017
34. Toteu, S. F.; PenayE, J.; Djomani, Y. P. Geodynamic evolution of the Pan-African belt in central Africa with special reference to Cameroon. Canadian Journal of Earth Sciences 2004, 41, 73-85. https://doi.org/10.1139/e03-079
35. Pin, C.; Poidevin, J.L. U-Pb zircon evidence for a pan-african granulite facies metamorphism in the Central African Republic. A new interpretation of the high-grade series of the northern border of the congo craton. Precambrian Res. 1987, 36, 303–312. https://doi.org/10. 1016/ 0301- 9268(87) 90027-1.
36. Nzenti, J.; Barbey, P.; MacaudierE, J.; Soba, D. Origin and evolution of the late Precambrian high-grade Yaounde gneisses (Cameroon). Precambrian research 1988, 38, 91-109. https://doi.org/10.1016/0301-9268(88)90086-1
37. Njanko, T.; Nédélec, A.; Affaton, P. Synkinematic high-K calc-alkaline plutons associated with the Pan-African Central Cameroon shear zone (W-Tibati area): petrology and geodynamic significance. Journal of African Earth Sciences 2006, 44, 494-510. https://doi.org/10.1016/j.jafrearsci.2005.11.016
38. Eboulement spectaculaire sur la route des gorges du Tarn. 2017. Available online : https://www.journaldemillau.fr/2017/03/08/un-eboulement-spectaculaire-sur-la-route-des-gorges-du-tarn/ (accessed on 12 March 2023)
39. Haute-Savoie : spectaculaire éboulement sur la départementale 22 à Vinzier, dans le Chablais. 2018. Available online: https://images.app.goo.gl/ci97cQee8MZbyWqL6 (accessed on 21 May 2023)
40. Road works on cracked Tarmac from subsidence. 2016. Available online : https://images.app.goo.gl/7pWM2E9HkamWFunS7 (accessed on 2 April 2023)
41. Colmaroute spécialiste du traitement fissures de chaussée. 2014. Available online : https://images.app.goo.gl/25gtcYSrZkgdeSqA8 (accessed on 21 July 2023)
42. Une route fissurée et déformée qui exaspère le maire et les habitants. 2017. Available online : https://images.app.goo.gl/mJUdXYF8Kmqv15t4A (accessed on 2 May 2023)
43. Effondremant de la route à Bifoun : le gouveernement se mobilise pour rétablir la situation. 2018. Available online : https://courierdesjournalistes.com/societe/effondrement-de-la-rote-a-bifoun-le-gouvernement-se-mobilise (accessed on 17 January 2023)
44. Nzenti, J.; Barbey, P.; Bertrand, J.; Macaudière, J. La chaîne panafricaine au Cameroun : cherchons suture et modèle. 1994. Abstracts 15eme RST, Nancy, Société Géologique France, édition Paris, 99.

45. Nzolang, C.; Kagami, H.; Nzenti, J. P.; Holtz, F. Geochemistry and preliminary Sr-Nd isotopic data on the Neoproterozoic granitoids from the Bantoum area, west Cameroon: evidence for a derivation from a Paleoproterozoic to Archaean crust. Polar Geosci. 2003, 16, 196-226. https://doi.org/10.15094/00003129
46. Njiosseu, E. L. T.; Nzenti, J.-P.; Njanko, T.; Kapajika, B.; Nédélec, A. New UPb zircon ages from Tonga (Cameroon): coexisting Eburnean–Transamazonian (2.1 Ga) and Pan-African (0.6 Ga) imprints. Comptes Rendus Geoscience 2005, 337, 551-562. https://doi.org/10.1016/j.crte.2005.02.005
47. Toteu, S.; Michard, A.; Bertrand, J., Rocci, G. U/Pb dating of Precambrian rocks from Northern Cameroon, orogenic evolution and chronology of the Pan-African belt of Central Africa. Precambrian Research 1987, 37, 71-87. https://doi.org/10.1016/0301-9268(87)90040-4
48. Penaye, J.; Toteu, S. F.; Michard, A.; Bertrand, J.-M.; Dautel, D. 1989. Reliques granulitiques d'âge protérozoïque inférieur dans la zone mobile panafricaine d'Afrique centrale au Cameroun; géochronologie U-Pb sur zircons. CR Acad. Sci. Paris 2003, 309, 315-318.
49. Toteu, S.; Van Schmus, W.; Penaye, J.; Michard, A. New U–Pb and Sm–Nd data from north-central Cameroon and its bearing on the pre-Pan African history of central Africa. Precambrian Research 2001, 108, 45-73. https://doi.org/10.1016/S0301-9268(00)00149-2
50. Ngako, V.; Affaton, P.; Njonfang, E. Pan-African tectonics in northwestern Cameroon: implication for the history of western Gondwana. Gondwana research 2008, 14, 509-522. https://doi.org/10.1016/j.gr.2008.02.002
51. Kankeu, B.; Greiling, R.O.; Nzenti, J.P.; Ganno, S.; Danguene, P.Y.E.; Bassahak, J.; Hell, J.V. Contrasting Pan-African structural styles at the NW margin of the Congo Shield in Cameroon. J. Afr. Earth Sci. 2018, 146, 28–47. https://doi.org/10. 1016/j.jafrearsci.2017.06.002
52. Shang, C. K.; Satir, M.; Siebel, W. TTG magmatism in the Congo craton; a view from major and trace element geochemistry, Rb-Sr and Sm-Nd systematic: case of Sangmelima region, Ntem complex, southern Cameroon. Journal of African Earth Sciences 2004, 40, 61-79.
53. Pouclet, A.; Tchameni, R.; Mezger, K.; Vidal, M.; Nsifa, N. E.; Penaye, P. Archaean crustal accretion at the northern border of the Congo Craton (South Cameroon). The charnockite-TTG link. Bull. Soc. Geol. Fr. 2007, 178, 3–14.
54. Takam, T.; Arima, M.; Kokonyangi, J.; Dunkley, D. J.; Nsifa, E. N. Paleoarchaean charnockites in the Ntem complex, Congo craton, Cameroon: insights from SHRIMP zircon U–Pb ages. J. Mineral. Petrol. Sci. 2009, 104, 1–11.
55. Tchameni, R.; Lerouge, C.; Penaye, J. ; Cocherie, A. ; Milesi, J. P. ; Toteu, S. F. ; Nsifa, E. N. Mineralogical constraint for metamorphic conditions in a shear zone affecting the Archean Ngoulemakong tonalite, Congo craton (southern Cameroon) and retentivity of U–Pb SHRIMP zircon dates. J. Afr. Earth Sci. 2010, 58, 67–80.
56. Lerouge, C.; Cocherie, A.; Toteu, S.F.; Penaye. J; Milesi, J.P., Tchameni, R., Nsifa, E.N.; Fanning, C. M.; Deloule, E. Shrimp U–Pb zircon age evidence for Paleoproterozoic sedimentation and 2.05 Ga syntectonic plutonism in the Nyong Group, South-Western Cameroon: consequences for the Eburnean–Transamazonian belt of NE Brazil and Central Africa. Journal of African Earth Sciences 2006, 44, 413–427.
57. Shang, C. K.; Satir, M.; Nsifa, E. N.; Liegeois, J. P.; Siebel, W.; Taubald, H. Archaean high K granitoids produced by remelting of the earlier Tonalite–Trondhjemite–Granodiorite (TTG) in the Sangmelima region of the Ntem complex of the Congo craton, southern Cameroon. Int. J. Earth Sci. 2007, 96, 817–842.
58. Carte routière du Cameroun. 2023. Available online: https://www.club-des-voyages.com (accessed on 21 May 2023)

59. Tchato, S.C.; Manguelle-Dicoum, E.; Njandjock, P.N. Notice explicative des routes principales en Afrique Centrale. Université de Yaoundé 1, Faculté de sciences, 2022.
60. Farr, T.G.; Kobrick, M. Shuttle Radar Topography Mission produces a wealth of data. Eos, Transactions American Geophysical Union 2000, 81,583-585. https://doi.org/10.1029/EO081i048p00583
61. USGS Earth explorer : Available online : https://earthexplorer.usgs.gov (accessed on 12 March 2020)
62. Gabr, S.; Ghulam, A.; Kusky, T. Detecting areas of high-potential gold mineralization using ASTER data. Ore Geology Reviews 2010, 38, 59-69. https://doi.org/10.1016/j.oregeorev.2010.05.007
63. Adiri, Z.; El Harti, A.; Jellouli, A.; Maacha, L.; Bachaoui, E. M. Lithological mapping using Landsat 8 OLI and Terra ASTER multispectral data in the Bas Drâa inlier, Moroccan Anti Atlas. Journal of Applied Remote Sensing 2016, 10, 016005. https://doi.org/10.1117/1.JRS.10.016005.
64. Amer, R.; Kusky, T.; El Mezayen, A. Remote sensing detection of gold related alteration zones in Um Rus area, Central Eastern Desert of Egypt. Advances in Space Research 2012, 49, 121-134. https://doi.org/10.1190/1.2387138
65. Zhang, X.; Pazner, M.; Duke, N. Lithologic and mineral information extraction for gold exploration using ASTER data in the south Chocolate Mountains (California). ISPRS Journal of Photogrammetry and Remote Sensing 2007, 62, 271-282. https://doi.org/10.1016/j.isprsjprs.2007.04.004
66. Touzi, R.; Lopes, A.; Bousquet, P. A statistical and geometrical edge detector for SAR images. IEEE Transactions on geoscience and remote sensing 1988, 26, 764-773. https://doi.org/10.1109/36.7708
67. Nezry, E.; Lopes, A.; Touzi, R. Detection of structural and textural features for SAR images filtering. IGARSS'91; Proceedings of the 11th Annual International Geoscience and Remote Sensing Symposium, Espoo, Finland. New York, Institute of Electrical and Electronics Engineers, Inc., p. 2169-2172. 1991. Available online: https://ieeexplore.ieee.org/document/575470 (accessed on 1 May 2022)
68. Lopes, A.; Nezry, E.; Touzi, R.; Laur, H. Structure detection and statistical adaptive speckle filtering in SAR images. International Journal of Remote Sensing 1993, 14, 1735-1758. https://doi.org/10.1080/01431169308953999
69. Binam, E. P. M.; Bidjeck, L. M. B.; Wambo, J. D. T.; Taku JR, A.,; Betsi, T. B.; Ipan, A. S.; Nfada, L. T.; Dieudonné, L. B. Lithologic and structural mapping of the Abiete–Toko gold district in southern Cameroon, using Landsat 7 ETM+/SRTM. Comptes Rendus Geoscience 2018, 350, 130-140. https://doi.org/10.1016/j.crte.2017.11.003
70. Kenea, N. Improved geological mapping using Landsat TM data, Southern Red Sea Hills, Sudan: PC and IHS decorrelation stretching. International Journal of Remote Sensing 1997, 18, 1233-1244. https://doi.org/10.1080/014311697218386
71. Suzen, M.; Toprak, V. Filtering of satellite images in geological lineament analyses: an application to a fault zone in Central Turkey. International journal of remote sensing 1998, 19, 1101-1114. https://doi.org/10.1080/014311698215621
72. Mallast, U.; Gloaguen, R.; Geyer, S.; Rödiger, T.; Siebert, C. Derivation of groundwater flow-paths based on semi-automatic extraction of lineaments from remote sensing data. Hydrology and Earth System Sciences 2011, 15, 2665-2678. https://doi.org/10.5194/hess-15-2665-2011
73. Abdelouhed, F.; Algouti, A.; Algouti, A.; Mlouk, M. A.; Ifkirne, M. Lithological mapping using Landsat 8 Oli multispectral data in Boumalne, Imider, and Sidi Ali Oubork, High Central Atlas, Morocco. E3S Web of Conferences 2021, 234, 00017. https://doi.org/10.1051/e3sconf/202123400017

74. Masoud, A.; Koike, K. Arid land salinization detected by remotely-sensed landcover changes: A case study in the Siwa region, NW Egypt. Journal of arid environments 2006, 66, 151-167. https://doi.org/10.1016/j.jaridenv.2005.10.011
75. Singh, K.; Arya, A. K.; Agarwal, K. K. Landslide Occurrences Along Lineaments on NH-154A, Chamba, Himachal Pradesh; Extracted from Satellite Data Landsat 8, India. Journal of the Indian Society of Remote Sensing 2020, 48, 791-803. https://doi.org/10.1007/s12524-020-01113-8
76. Yao, T.K. ; Oya, Y.M.S. ; Olivier, F. ; Assoma, V. Extraction de linéaments structuraux à partir d'images satellitaires, et estimation des biais induits, en milieu de socle précambrien métamorphisé. Revue Teledetection 2012, 10, 161-178. https://doi.org/10.17184/eac.10287736v10n4
77. Singhal, B. B. S.; Gupta, R. P. Applied hydrogeology of fractured rocks, Springer Science & Business Media. 2010. Available online: https://link.springer.com/book/10.1007/978-90-481-8799-7 (accessed on 9 April 2023)
78. Li, N. Textural and rule-based lithological classification of remote sensing data, and geological mapping in Southwestern Prieska sub-basin. Transvaal Supergroup, South Africa. lmu. 2010, 60, 237-246. https://doi.org/10.5282/edoc.11824
79. Nkono, C.; FéméniaS, O.; Lesne, A.; Mercier, J.-C.; Demaiffe, D. Fractal Analysis of lineaments in Equatorial Africa: insights on lithospheric structure. Open Journal of Geology 2013, 3. https://doi.org/10.4236/ojg.2013.33019
80. Actualités IRGM : Séisme dans plusieurs localités du Cameroun. 2019. Available online: https://www.irgm-cameroun.org/actualites (accessed on 15 December 2022)
81. Manguelle, E.D., Bokosah, A.S.; Kwende-Mbanwi, T.E. Geophysical evidence for a major Precambrian schist-granite boundary in southern Cameroon. Tectonophysics 1992, 205, 437-446.
82. Gweth, M.M.A.; Meli'i, J.L.; Oyoa, V.; Diab, A.D.; Gouet, D.H.; Jean, M.; Njandjock, P.N. Fracture network mapping using remote sensing in three crater lakes environments of the Cameroon volcanic line (central Africa). Arabian Journal of Geosciences 2021b, 14, 422. https://doi.org/10.1007/s12517-021-06762-8.
83. Cheunteu, C. A. F.; Adiang, C. M.; Pemi, M. M.; Tokam, A. P. K.; Nouayou, R.; Nguiya, S. Mapping of major tectonic lineaments across Cameroon using potential field data. Earth, Planets and Space 2022, 74,59. https://doi.org/10.1186/s40623-022-01612-7.
84. Nguimbous-Kouoh, J.J.; Manguelle-Dicoum, E. Contribution of topographic and penetrometric measurements to a site characterization, case of the Kekem landslide, National road N$^{0}$5 (western Cameroon). Earth Sci. Res. 2010, J., 14, 2.
85. Pouyon, D. E.; Ganno, S.; Tabod, C. T. Geophysical and Geotechnical Investigations of a Landslide in Kekem Area, Western Cameroon. International Journal of Geosciences 2012, 3, 780-789. http://dx.doi.org/10.4236/ijg.2012.34079.